Homogenization of two-dimensional materials integrating monolayer bending and surface layer effects

Huichao Liu [a], Yan Chen [a,*], Wen Wang [b], Luqi Liu [c,d], Yilun Liu [a,*], Quanshui Zheng [e,f,g,h,i]

[a] *Laboratory for multiscale mechanics and medical science, SV LAB, School of Aerospace, Xi'an Jiaotong University, Xi'an 710049, China*
[b] *School of Mechanical Engineering, Southwest Jiaotong University, Chengdu 610031, China*
[c] *CAS Key Laboratory of Nanosystem and Hierarchical Fabrication and CAS Center for Excellence in Nanoscience, National Center for Nanoscience and Technology, Beijing, China*
[d] *University of Chinese Academy of Sciences, Beijing, China*
[e] *Center for Nano and Micro Mechanics, Tsinghua University, Beijing 100084, China*
[f] *Department of Engineering Mechanics, School of Aerospace Engineering, Tsinghua University, Beijing 100084, China*
[g] *State Key Lab of Tribology in Advanced Equipment (SKLT), Tsinghua University, Beijing 10084, China*
[h] *Institute of Superlubricity Technology, Research Institute of Tsinghua University in Shenzhen, Shenzhen 518057, China*
[i] *Tsinghua Shenzhen International Graduate School, Shenzhen 518057, China*

ARTICLE INFO

ABSTRACT

Two-dimensional (2D) materials hold great promise for future electronic, optical, thermal devices and beyond, underpinning which the predictability, stability and reliability of their mechanical behaviors are the fundamental prerequisites. Despite this, due to the layered crystal lattice structure, extremely high anisotropy and the independent deformation mechanism of out-of-plane bending, the proper homogenization for such materials still faces challenge. That is because the monolayer bending is of independent deformation mechanism distinct from the traditional bulk deformation which thereby brings couple stress to the bulk 2D materials, while the different interlayer constraints of bulk and surface layers bring surface layer effect. In this paper, by considering the two effects, a continuum mechanics framework for extremely anisotropic 2D materials (CM2D) is proposed, without necessities of ad hoc experiments for the unclassical parameters. Under the framework of the CM2D, beam-like deformation, plate-like deformation and indentation of 2D materials are studied to showcase its ability and applicability. An analytical expression of the effective bending rigidity is derived, which can be characterized by several dimensionless parameters. It is found that the overall bending deformations of 2D materials are controlled by the competition between the intralayer deformation mode and the interlayer shear deformation mode. Besides, the size-dependent modulus is also identified on the indentation of 2D materials at the pure elastic deformation regime, distinct from the size effect caused by plasticity. In addition, we discussed the effects of monolayer bending and surface layer on the mechanical behaviors of 2D materials. Our work not only provides guidance for the studies and applications of 2D materials, but also serves as a good example with well-defined physical meanings for the strain gradient, high-order moduli and couple stress in high-order continuum mechanics theories.

* Corrresponding authors.
E-mail addresses: yanchen@xjtu.edu.cn (Y. Chen), yilunliu@mail.xjtu.edu.cn (Y. Liu).

1. Introduction

Multilayer two-dimensional (2D) materials can be regarded as a stack of monolayer 2D material sheets, such as graphene, hexagonal boron-nitride (h-BN), transition metal-dichalcogenides, transition metal carbides and nitrides (MXenes), inorganic semiconductors, etc., in a layer-by-layer manner. Thanks to their excellent and exotic physical properties (Lee et al., 2008; Z. Liu et al., 2012; Cao et al., 2018; Ares et al., 2020; Deng et al., 2020; Autere et al., 2018; Kim et al., 2021), 2D materials hold great promise in electronic, optical, thermal devices and beyond. Furthermore, they can serve as a powerful and robust platform for exploring the manipulation of material properties through methods such as strain engineering(Dai et al., 2019), symmetry engineering(Du et al., 2021), interfacial engineering(Yu et al., 2021) and modular assembly(Geim and Grigorieva, 2013; Liu et al., 2016; Novoselov et al., 2016). Underpinning these applications, the predictability, stability and reliability of mechanical behaviors are the prerequisites (Akinwande et al., 2017; Hou et al., 2024; Rafii-Tabar et al., 2016).

Although there are many types of 2D materials with various structures, the common mechanical features are conspicuous, i.e., individual layer is connected by strong chemical bonds, while the adjacent layers are held together by relatively weak van der Waals (vdW) interactions (see e.g., Fig. 1), yielding strong intralayer yet weak interlayer stiffness and strength(Wang and Zheng, 2007; Wang et al., 2017; Chen et al., 2015; Shen and Wu, 2012). Besides, unlike classical materials, the monolayer constituent exhibits quite different deformation mechanism in the atomic view(Ru, 2000). For example, the intralayer deformation of graphene only concerns the stretches and bending of σ bond, while its out-of-plane bending involves the deformation of π bond, i.e., the torsional misalignment between the neighboring p_z orbitals (see Fig. 1c)(DiBiasio et al., 2007; Lu et al., 2009; Zhang et al., 2011). This discrepancy gives rise to different energetic mechanisms governing the deformation of individual 2D monolayers, thereby leading to decoupled intralayer stiffness and out-of-plane bending rigidity. Consequently, the attempt to correlate the stiffness of the two deformation modes through effective thickness and Young's modulus just like classical plate unavoidably leads to contradictories in 2D materials(Huang et al., 2006; Shenderova et al., 2002; Wang and Zhang, 2008). Moreover, the internal layers and outmost layers are under different interlayer constraints or coordination environments (see Fig. 1d). That is the internal layer has two neighbors on both sides, while an outmost layer only has one neighbor on its single side to interact with. Up to now, many methods have been proposed to study the mechanical
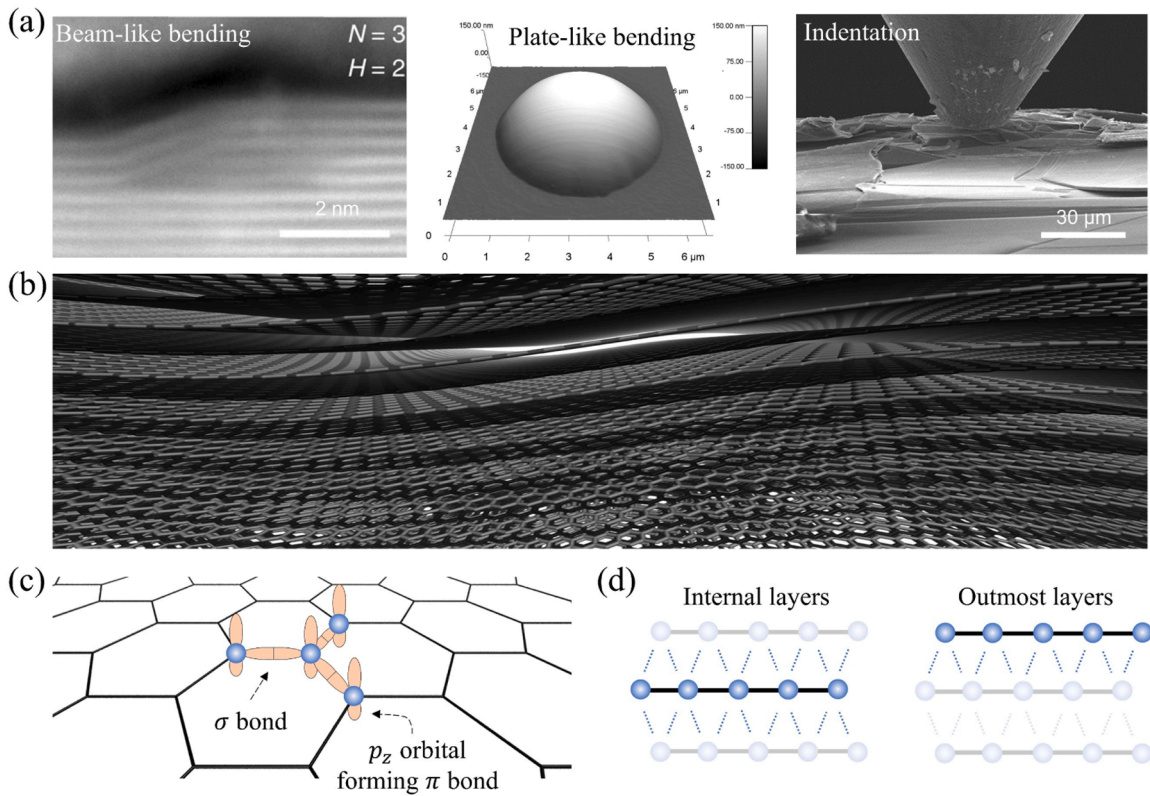
Fig. 1. The atomic essence of complex deformations in 2D materials. (a) Three typical deformations of graphene observed in experiments: beam-like bending of a 3-layer graphene sheet over a 2-layer h-BN step(Han et al., 2019), plate-like bending (bulged bubble) of graphene, and indentation of multilayer graphene flakes (b) Atomistic model of multilayer graphene deformation composed of discrete monolayer deformation. (c) Schematic illustrations of the σ bonds (accounting for intralayer deformation) and π bond (related to the out-of-plane bending of monolayer) (d) Schematic illustrations of interlayer vdW interactions, which also exhibits the origin of surface layer effect where interlayer constraints or coordination environments for outmost layers are distinct from internal layers.

behaviors of 2D materials, such as molecular dynamics (MD) simulations and first-principle calculations, etc. However, theses atomistic models are usually limited to small scales, due to their notoriously high degrees of freedom.

Thus, more efficient continuum mechanics theories for 2D materials are strongly desired, which treat materials as continua and involve only a limited number of variables or fundamental unknowns to deal with. Developing an atomistic-based continuum model that correlates with atomistic configuration might be the first instinct to address the unique features of 2D materials. Indeed, inspired by the atomistic models, the interatomic potential is incorporated into a continuum model through the Cauchy-Born rule and equivalence of strain energy and interatomic potential energy(Zhang et al., 2002; Arroyo and Belytschko, 2002). Subsequently, continuum mechanics models based on various interatomic potentials are proposed for single-walled nanotubes or monolayer 2D materials(Zhang et al., 2004; Arroyo and Belytschko, 2004a; Guo et al., 2006; Yadav and Ghosh, 2022). In comparison, the incorporation of interlayer interaction into the atomistic-based proposal turns out to be considerably challenging, because the map between macro-strain and interlayer relative motion is not properly established. Thus, a simplified cohesive model is employed by only considering the interlayer distance(Arroyo and Belytschko, 2004b; Lu et al., 2007), which neglects the interlayer shear resistance. Similar interlayer consideration is integrated into the foliation model for multilayer 2D materials(Ghosh and Arroyo, 2013). Merely with atomistic configurations and interatomic potentials, atomistic-based models intend to bridge the continuum mechanics model with their atomistic bases. Nevertheless, the implementation is highly complicated and has to be re-formulated for different atomistic lattice structures or for different forms of interatomic potentials. Thus, the development of a more simplified continuum mechanics model but with sufficient precision for general 2D materials is eagerly desirable.

On the other hand, the effective continuum mechanics models may appear to be phenomenological compared to their atomistic-based counterparts, but they offer an alternative approach to circumvent the reliance on specific lattices or interatomic potentials. For 2D materials, low-dimensional continuum models such as beam, membrane and plate have been abstractly established, with material parameters determined through simple experiments or simulations. For example, a multibeam shear model(Liu et al., 2011) regards each layer of multilayer 2D materials as a beam, with interlayer filled with media only accounting for shear deformation energy. On the other hand, by neglecting the out-of-plane bending, the deformable tension shear chain model for 2D material-based nacre-like structures was developed (Liu et al., 2012; Liu and Xu, 2014; He et al., 2019). To directly address monolayer bending effect, an independent monolayer bending rigidity is assigned to each layer(Yue et al., 2012), leading to the modified Timoshenko beam model (Qin et al., 2020). However, all the above-mentioned bending models are constrained by the planar cross-section assumption, which is then discarded in the study of the bending rigidity of 2D material beams(Ma et al., 2020; Chen et al., 2023) and plates(Ma et al., 2022) by solving the intralayer equilibrium equations of each layer on equal-curvature configuration. Furthermore, a more general beam theory for 2D materials, which is not bound to equal curvature but still maintains incompressibility of thickness, is developed(Huang et al., 2023) by coupling the in-plane equilibrium equation of each layer with bending deformation. Furthermore, by treating the in-plane displacement as a continuous function along the thickness coordinate, the entire equilibrium equations of each layer can be simplified as several partial differential equations, so that the analytical solution for large layer number becomes feasible. Nonetheless, their operation of continualization is purely mathematical and the complete three-dimensional (3D) deformation is also not considered. So far, the effective continuum mechanics models mainly focus on low dimensional structure models and are stuck in 'unchanged thickness' assumptions. It is hard for them to deal with 3D deformation scenarios, like indentation.

In addition, for micro- and nano- materials, size effects are highly significant and often dominate their unique mechanical behaviors. Hitherto, many general continuum mechanics theories have been proposed to address such features. For example, the surface effect model(Gurtin and Ian Murdoch, 1975; Huang and Wang, 2006; Wang and Feng, 2007) treats the internal volume and the surface as different materials with different material parameters, so that the size changes the specific surface area and thus the overall response of the material. Another example is the high-order continuum mechanics model(Toupin, 1962; Mindlin and Eshel, 1968), which employs the higher order gradients of displacement or gradients of strain as deformation measures in addition to the strain. Some of the versions are also known as strain gradient theory(Fleck and Hutchinson, 1997; Wei, 2001) or couple stress theory(Yang et al., 2002; Hadjesfandiari and Dargush, 2011). This kind of theories exhibits size dependent mechanical behaviors, because the additional high-order deformation measures are no longer dimensionless. Some more theories are discussed in the comprehensive review (Srinivasa and Reddy, 2017). Despite these generally formulated theories, some of the material parameters don't have clear physical meaning and are also hard to measure in experiments which hinders the wide application of these theories. However, the unique features of 2D materials provide a good testbed to verify the non-classic continuum mechanics theories. But, up to now the continuum mechanics theory applicable to the general deformation of 2D materials is still lacking.

In this work, we propose a continuum mechanics framework for 2D Materials (CM2D), which is transversely isotropic integrating monolayer bending and surface layer effects. The layout of this paper is as follows. In Section 2, the general 3D form of the CM2D is formulated and the differences with the previous high-order continuum mechanics and surface effect model are also elucidated. In Section 3, the mechanical behaviors of beam-like, plate-like deformation and indentation of 2D materials, are studied under the framework of the CM2D. In Section 4, the monolayer bending and surface layer effects on effective bending stiffness of 2D materials are systematically discussed. Finally, the conclusion remarks are given in Section 5.

2. Continuum mechanics framework for 2D materials

In this section, the general 3D form of the CM2D is first formulated, followed by some comparison and comments. Suppose n layers of 2D material sheets are initially stacked parallel to the x-o-y plane with a distance of t. The total thickness is given by $h = (n-1)t$. The intralayer deformation of individual 2D material sheet, e.g., graphene as illustrated in Fig. 1c, consists of the length and angle changes of σ bonds, while its out-of-plane bending mainly concerns the deformation of the π bond. As a result, we assign independent

intralayer parameters (i.e., 2D Young's modulus E_{2D} and Poisson's ratio ν_p) and bending parameters (i.e., bending rigidity D_m and Gaussian bending rigidity D_g) to the continuous 2D material sheets. Besides, the interlayer interaction originating from vdW interactions provides the resistance of interlayer shearing and out-of-plane tension/compression (see Fig. 1d), which are depicted by the interlayer continuous media with corresponding shear modulus G_t and Young's modulus E_t. All these parameters can be determined through fundamental experiments or molecular dynamics (MD) simulations. Take h-BN as an example, the mechanical parameters are obtained by using Tersoff potential(Kınacı et al., 2012) for intralayer interactions and ILP potential(Ouyang et al., 2018) for interlayer interactions in the large-scale atomic/molecular massively parallel simulator (LAMMPS), as shown in Table 1.

Only the $(n-2)$ internal layers measured $h_{in} = (n-2)t$ in thickness (the part between the two surfaces represented by black dot lines in the middle and right panels of Fig. 2a) are homogenized, which will be referred to as the 'bulk' part thereafter. The in-plane parameters of the 'bulk' part are $\overline{E}_{2D} = E_{2D}/t$ and ν_p. The transverse Young's modulus is E_t and shear modulus G_t. In addition to this depiction of standard transversely isotropic materials, the homogenized bending moduli, i.e., $\overline{D}_m = D_m/t$ and $\overline{D}_g = D_g/t$, naturally emerge from the independent monolayer sheet bending rigidities. Note that in our model, the bulk bending moduli have a clear physical origin. They are directly related to the bending rigidity of monolayer 2D material sheets.

The outmost 2D material sheets together with the rest adjacent half interlayers (the parts outside the two surfaces represented by black dot lines in the middle and right panels of Fig. 2a) are reserved, which will be referred to as the 'surface' part thereafter. The 'surface' part needs special treatment, because each outmost sheet has adjacent sheets only at its single side to interact with, while its internal counterparts have adjacent sheets at both sides (Fig. 1d). Note that there is a distance of $t/2$ between the outmost 2D material sheets and the 'bulk' part, filled by interlayer media. By retaining $t/2$ interlayer media layers with the outmost 2D material sheets, each internal 2D material sheet can be regarded as situated in the middle of two $t/2$ interlayer media layers.

Denote the 'bulk' part displacement by u_i, and its deformation is measured by strain

$$\varepsilon_{ij} = \frac{1}{2}\left(u_{i,j} + u_{j,i}\right) \tag{1a}$$

and the additional 'bulk' part curvature (related to sheet curvature)

$$\kappa_{\alpha\beta} = w_{,\alpha\beta} \tag{1b}$$

where we denote $w = u_3$ for discrimination. The Latin letters in subscripts represent the indexes of full 3D dimensions, e.g. taking values from $\{x,y,z\}$, while the Greek letters are the ones of in-plane 2D dimensions, e.g. taking values from $\{x,y\}$. The comma denotes derivative, i.e., $(\ )_{,i} = \partial/\partial x_i$. Note that Eq. (1b) is also part of the high-order gradient of displacement.

The 'surface' part displacement is denoted by $u_i^{(j)}$, where the superscript $j = 1$, n respectively representing the bottom and top layers, is independent of the subscript. The in-plane strain and sheet curvature are expressed as

$$\varepsilon_{\alpha\beta}^{(i)} = \frac{1}{2}\left(u_{\alpha,\beta}^{(i)} + u_{\beta,\alpha}^{(i)}\right) \tag{2a}$$

$$\kappa_{\alpha\beta}^{(i)} = w_{,\alpha\beta}^{(i)} \tag{2b}$$

The transverse strain of the 'surface' part actually belongs to the half layer of interlayer media, which is assumed to be uniform along z-axis, and expressed by the displacements of neighboring outmost 2D material sheet and the interfaces of the 'bulk' part, as

$$\varepsilon_{\alpha3}^{(i)} = \frac{1}{2}\left(\frac{u_\alpha^{(i)} - u_\alpha}{t/2}n^{(i)} + \frac{w_{,\alpha}^{(i)} + w_{,\alpha}}{2}\right) \tag{2c}$$

$$\varepsilon_{33}^{(i)} = \frac{(w^{(i)} - w)n^{(i)}}{t/2} \tag{2d}$$

where u_α, w and $w_{,\alpha}$ are evaluated at the boundaries of the 'bulk' part $z = \pm h_{in}/2$ and $n^{(1)} = -1$, $n^{(n)} = 1$ are introduced for compactness. The first term in Eq. (2c) is a difference quotient to approximate the derivatives of in-plane displacement components along thickness direction. The second term is a simple average of $w_{,\alpha}^{(i)}$ and $w_{,\alpha}$ to approximate the derivative of out-of-plane displacement component along in-plane direction.

For the 'bulk' part, the homogenized constitutive relationships are

Table 1
Mechanical parameters of h-BN determined through MD simulations.

	E_{2D} (GPa·nm)	ν_p	D_m (eV)	D_g (eV)	G_t (GPa)	E_t (GPa)	t (nm)
Values	247.3	0.3051	0.8738	1.57*	7.655	37.35	0.3201

* Note: the value of Gaussian bending rigidity has been calculated by DFT (1.52 eV)(Wei et al., 2013) and atomistic potential based continuum mechanics model (1.62 eV) (Davini et al., 2017). Here, we take the average of the two.
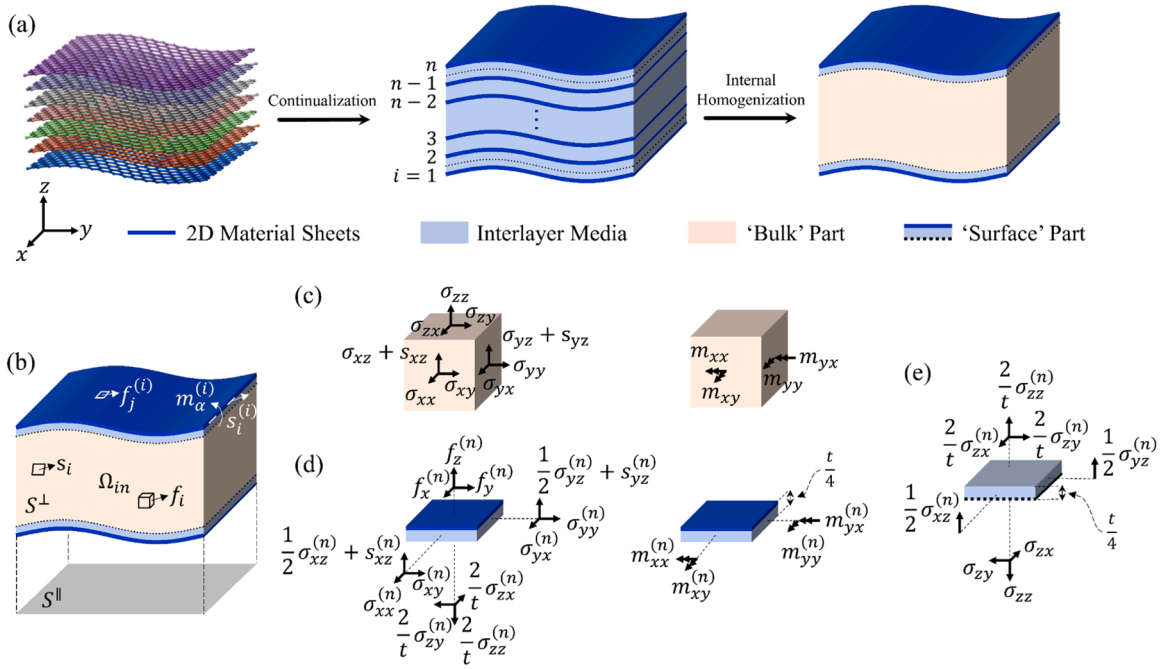
Fig. 2. (a) The schematic illustration of continualization and homogenization from 2D material (the left panel) to its multilayer continuum model (the middle panel) and its internal homogenized model (the right panel). (b) External loads applied on a CM2D solid. (c) Stress and couple stress borne by the 'bulk' part element (the body force is masked). (d) Surface stress, stress, bending moment and external traction borne by the outer half of the topmost 'surface' part element. (e) Surface stress and stress borne by the inner half of the topmost 'surface' part element. Please note that not all stress components and things like that are shown, for the sake of conciseness. (b)~(e) only schematically exhibit which element surfaces the stress components, couple stress components, etc. are applied on.

$$\sigma_{\alpha\beta} = \frac{\overline{E}_{2D}\nu_p}{1-\nu_p^2}\varepsilon_{\gamma\gamma}\delta_{\alpha\beta} + \frac{\overline{E}_{2D}}{1+\nu_p}\varepsilon_{\alpha\beta} \tag{3a}$$

$$\sigma_{\alpha3} = 2G_t\varepsilon_{\alpha3} \tag{3b}$$

$$\sigma_{33} = E_t\varepsilon_{33} \tag{3c}$$

$$m_{\alpha\beta} = \left(\overline{D}_m - \overline{D}_g\right)\kappa_{\gamma\gamma}\delta_{\alpha\beta} + \overline{D}_g\kappa_{\alpha\beta} \tag{3d}$$

where the dummy index convention and 2D Kronecker delta $\delta_{\alpha\beta}$ are adapted for convenience, unless otherwise specified. σ_{ij} is the symmetric part component of the stress tensor. Note that, the Poisson coupling between in-plane and transverse deformations is ignored (see Eq. (3c)) due to the weak interlayer interaction. Moreover, the bulk curvature $\kappa_{\alpha\beta}$ naturally emerges from the distinctive sheet bending of 2D materials (Eq. (3d)). Thus, its work conjugate, i.e., the couple stress $m_{\alpha\beta}$ have clear physical meanings in this homogenized model. They are directly related to the 2D material sheet curvature and the moment that drives such curvature, respectively. In addition, the bulk bending moduli $\overline{D}_m$ and $\overline{D}_g$ are directly related to the bending stiffness of monolayer 2D material sheets.

For the 'surface' part, the constitutive relationships of in-plane deformations and surface bending are the same as those of a monolayer 2D material sheet, i.e.,

$$\sigma_{\alpha\beta}^{(i)} = \frac{E_{2D}\nu_p}{1-\nu_p^2}\varepsilon_{\gamma\gamma}^{(i)}\delta_{\alpha\beta} + \frac{E_{2D}}{1+\nu_p}\varepsilon_{\alpha\beta}^{(i)} \tag{4a}$$

$$m_{\alpha\beta}^{(i)} = \left(D_m - D_g\right)\kappa_{\gamma\gamma}^{(i)}\delta_{\alpha\beta} + D_g\kappa_{\alpha\beta}^{(i)} \tag{4b}$$

Since the transverse surface strain is assumed to be uniform along thickness, the constitutive relationship is therefore directly integrated out along z, resulting in

$$\sigma_{\alpha3}^{(i)} = G_t t\varepsilon_{\alpha3}^{(i)} \tag{4c}$$

$$\sigma_{33}^{(i)} = \frac{1}{2}E_t t \varepsilon_{33}^{(i)} \tag{4d}$$

Note that $\varepsilon_{kl}^{(i)}$ and $\kappa_{\alpha\beta}^{(i)}$ still adhere to the classical definitions of strain and curvature, respectively. And $m_{\alpha\beta}^{(i)}$ is the bending moment of plate elements. By comparison, $\sigma_{kl}^{(i)}$ is surface stress component. It has the dimension of stress multiplied by length (e.g., with the unit of GPa·nm). Thus, the whole model can be formally regarded as a homogenous material with extra layers attached to its transverse boundaries.

To derive the equilibrium equations, the virtual work principle is adapted as

$$\int_{\Omega_{in}} \sigma_{ij}\delta\varepsilon_{ij}\mathrm{d}\Omega_{in} + \int_{\Omega_{in}} m_{\alpha\beta}\delta\kappa_{\alpha\beta}\mathrm{d}\Omega_{in} + \int_{S^{\parallel}} \sigma_{ij}^{(i)}\delta\varepsilon_{ij}^{(i)}\mathrm{d}S + \int_{S^{\parallel}} m_{\alpha\beta}^{(i)}\delta\kappa_{\alpha\beta}^{(i)}\mathrm{d}S = \int_{\Omega_{in}} f_i\delta u_i\mathrm{d}\Omega_{in} + \int_{S^{\perp}} s_i\delta u_i\mathrm{d}S + \int_{S^{\perp}} m_\alpha\delta w_{,\alpha}\mathrm{d}S + \int_{S^{\parallel}} f_j^{(i)}\delta u_j^{(i)}\mathrm{d}S + \int_{\partial S^{\parallel}} s_i^{(i)}\delta u_i^{(i)}\mathrm{d}s$$
$$+ \int_{\partial S^{\parallel}} m_\alpha^{(i)}\delta w_{,\alpha}^{(i)}\mathrm{d}s \tag{5}$$

where Ω_{in} represents the 3D domain of the 'bulk' part (see Fig. 2b), $S^{\parallel}$ the 2D domain projected by the 2D material sheets to their initial parallel plane, and $S^{\perp}$ the transverse surface of the 'bulk' part initially perpendicular to the 2D material sheets. The terms on the left-hand side of Eq. (5) represent the internal virtual work related to the virtual strains and curvatures of the 'bulk' part and the 'surface' part, while the ones on the right-hand side represent the external virtual work related to the virtual displacements and bending angles. f_i is the external volume force applied to Ω_{in}, and s_i is the external traction applied on $S^{\perp}$. $f_j^{(i)}$ is the external traction applied on the 'surface' part, or to be specific, on the outmost 2D material sheets. $s_j^{(i)}$ and $m_\alpha^{(i)}$ is the external forces and moments applied on the edges of the outmost 2D material sheets, respectively. Note that, the superscripts are not forced to dummy index convention. Instead, they are bound by another convention for the sake of conciseness, i.e., the integrand in Eq. (5) needs to be summed over the two outmost surfaces, as long as there is a superscript. For example, in the integrand, $a^{(i)}b^{(i)} = a^{(1)}b^{(1)} + a^{(n)}b^{(n)}$ and $a^{(i)}b = a^{(1)}b|_{z=-h_{in}/2} + a^{(n)}b|_{z=h_{in}/2}$.

Then, we can derive the equilibrium equations by the principle of variation, as detailed in S2 of the Supplementary Information. As a result, in Ω_{in}, we have

$$\sigma_{\alpha j,j} + f_\alpha = 0 \tag{6a}$$

$$\sigma_{3j,j} - m_{\alpha\beta,\alpha\beta} + f_3 = 0 \tag{6b}$$

On the 'surface' part, we have

$$\left(\sigma_{\alpha\beta,\beta}^{(i)} + f_\alpha^{(i)} - \frac{2n^{(i)}}{t}\sigma_{\alpha3}^{(i)}\right)\delta u_\alpha^{(i)} = 0 \tag{7a}$$

$$\left(\frac{1}{2}\sigma_{\alpha3,\alpha}^{(i)} - \frac{2n^{(i)}}{t}\sigma_{33}^{(i)} - m_{\alpha\beta,\alpha\beta}^{(i)} + f_3^{(i)}\right)\delta w^{(i)} = 0 \tag{7b}$$

$$\left(\sigma_{\alpha3}n_3 - \frac{2n^{(i)}}{t}\sigma_{\alpha3}^{(i)}\right)\delta u_\alpha = 0 \tag{7c}$$

$$\left(\sigma_{33}n_3 - \frac{1}{2}\sigma_{\alpha3,\alpha}^{(i)} - \frac{2n^{(i)}}{t}\sigma_{33}^{(i)}\right)\delta w = 0 \tag{7d}$$

On the surfaces of the 'bulk' part initially perpendicular to the 2D material sheets, i.e., $S^{\perp}$, we have

$$\left(\sigma_{\alpha\beta}n_\beta - s_\alpha\right)\delta u_\alpha = 0 \tag{8a}$$

$$\left(\sigma_{3\beta}n_\beta - m_{\alpha\beta,\beta}n_\alpha - s_3\right)\delta w = 0 \tag{8b}$$

$$\left(m_{\alpha\beta}n_\beta - m_\alpha\right)\delta w_{,\alpha} = 0 \tag{8c}$$

On the edges of the 'surface' part, we have

$$\left(\sigma_{\alpha\beta}^{(i)}n_\beta - s_\alpha^{(i)}\right)\delta u_\alpha^{(i)} = 0 \tag{9a}$$

$$\frac{1}{2}\sigma_{\alpha3}^{(i)}n_\alpha\delta w = 0 \tag{9b}$$

$$\left(\frac{1}{2}\sigma_{\alpha3}^{(i)}n_\alpha - m_{\alpha\beta,\beta}^{(i)}n_\alpha - s_3^{(i)}\right)\delta w^{(i)} = 0 \tag{9c}$$

$$\left(m_{\alpha\beta}^{(i)}n_\beta - m_\alpha^{(i)}\right)\delta w_{,\alpha}^{(i)} = 0 \tag{9d}$$

where n_i is the component of the unit outward normal vector of the considered surface. Eqs. (6) are the equilibrium conditions of a 'bulk' part element (Fig. 2c). Different from the standard bulk equilibrium equations, an additional term naturally emerges from the independent sheet bending in Eq. (6b). This additional term is related to the asymmetric part of the stress tensor $s_{\alpha3} = -m_{\beta\alpha,\beta}$, which is expressed in terms of couple stress using the moment balance conditions (see S3.1 in the Supplementary Information). Eq. (7a) and Eq. (7b) are the equilibrium conditions of the outer half of the outmost 'surface' part element (see Fig. 2d for the outer half of the topmost 'surface' part element as an example). Eq. (7c) and Eq. (7d) are the equilibrium conditions of the inner half of the outmost 'surface' part element (see Fig. 2e for the inner half of the topmost 'surface' part element as an example), which actually provide the coupling relationships between the 'bulk' part and the 'surface' part. The equilibrium conditions of the 'surface' part element have to be expressed in two parts, i.e., the outer and inner parts, because we take the average of $w_{,\alpha}^{(i)}$ and $w_{,\alpha}$ to approximate the derivative of out-of-plane displacement component along in-plane direction (see Eq. (2c)). The detailed derivation of Eqs. (6) and (7) from the viewpoint of element equilibrium can be found in S3 of the Supplementary Information.

Eqs. (6)~(9) are the general governing equations and boundary conditions of the continuum mechanics framework for 2D materials (CM2D). Overall, the proposed CM2D model is transversely isotropic, featuring surface elasticity and high-order displacement gradient terms. Here, we make some remarks regarding the two unclassical features.

Surface elasticity has been well identified by the widely accepted standard surface effect model(Gurtin and Ian Murdoch, 1975; Huang and Wang, 2006; Wang and Feng, 2007). It is motivated by such idea that compared to their bulk counterparts, atoms in surfaces or interfaces of materials usually possess different coordination environments, charge distributions and lattice constants, etc., leading to mismatches and extra interactions with the atoms in bulk region. This renders different energy structures and stiffness to the surface and the bulk(Javili et al., 2013; Mozaffari et al., 2020). Due to the strong chemical bonds in the 3D crystal lattices, creating a fresh surface by removing part of the material can drastically disturb the original equilibrium state and drag the original crystal structure into reconstruction, leading to a severe distortion of the surface lattice and the development of residual stress. Therefore, for traditional 3D crystals, it is sound to treat the surface and the bulk regions differently. However, in our model, although the 'surface' part and the 'bulk' part are also treated differently, nevertheless, the underpinning physical ideas are mainly related to the different vdW coordination environments. It only makes each outmost layer interact with the rest layers differently from its internal counterparts. Since the vdW interaction is pretty weak, the disturbances of changed coordination environments to the crystal structure of the outmost layers are negligible. As shown in Fig. S1, the residual stress of multilayer graphene is almost inappreciable compared with materials with a 3D crystal lattice, like the face-centered cubic Au. Hence, all the layers still share the same elastic parameters, unlike the standard surface effect model, where the surface elasticity parameters need to be determined through ad hoc experiments.

High-order displacement gradients have been also employed as additional deformation measures in high-order continuum mechanics theories(Toupin, 1962; Mindlin and Eshel, 1968), such as couple stress theories(Yang et al., 2002; Hadjesfandiari and Dargush, 2011). The comparison is made as follows. First, the definition of curvature is different. In couple stress theories, the curvature is usually defined as the symmetric part or the skew symmetric part of the gradient of rotation vector. The latter is related to the curl of the displacement field. By comparison, the definition of curvature in the CM2D model is inherited from the plate theory, which is simply the in-plane second-order gradient of the out-of-plane displacement component and is physically plausible. This leads to another difference that the curvature tensor is a 2D tensor in the CM2D model instead of a 3D one as in the couple stress theory. Besides, although these high-order gradients in high-order continuum mechanics theories are usually interpreted as curvature or torsion, their connection to a specific micro- or atomic structure remains subtle(Neff et al., 2016; Shaat et al., 2020; Srinivasa and Reddy, 2017). In the CM2D model, otherwise, the bulk curvature is directly related to the 2D material sheet bending curvature. The physical picture in the atomic view is clear. Moreover, unlike the CM2D model, the additional stiffness parameters related to high-order terms in high-order continuum mechanics theories usually need to be determined through ad hoc experiments.

Although an analytical solution may be feasible in certain simplified scenarios, it is hard to obtain in general. But through the finite element method, which can be conveniently implemented via, e.g., the weak-form-PDE module in COMSOL Multiphysics® (COMSOL), we can always obtain the numerical solutions. In Section 3, we will give some typical solutions under the framework of the CM2D model.

3. Solution of the CM2D model

In this section, some fundamental classical mechanics models, such as beam, plate and indentation, are re-considered within the framework of the present CM2D model. These elementary problems are taken as examples to demonstrate the applicability of our CM2D model and explore the typical deformation behaviors of 2D materials.

3.1. Beam model of 2D materials

3.1.1. Beam model within the CM2D framework

To derive a beam model, consider beam-like bending of the multilayer 2D materials within x-o-z plane. The Greek subscript takes value x, and the Latin one takes values from $\{x,z\}$. The components of displacement u_x and u_z will be denoted by u and w for simplicity. The dummy index convention is abandoned in this subsection.

Neglecting external volume force f_i, and integrating Eq. (6b) along the thickness of the 'bulk' part, we arrive at

$$\sigma_{zz}\big|_{z=\frac{h_{in}}{2}} - \sigma_{zz}\big|_{z=-\frac{h_{in}}{2}} = \int_{-\frac{h_{in}}{2}}^{\frac{h_{in}}{2}} \left(-\sigma_{zx,x} + m_{xx,xx} \right) \mathrm{d}z \tag{10}$$

Based on Eq. (7a), the in-plane displacement of the 'surface' part is expressed as

$$u^{(i)} = u + n_z \frac{t}{2}\left(u_{,z} + w_{,x}\right) - \frac{t}{4n^{(i)}}\left(w_{,x}^{(i)} + w_{,x}\right) \tag{11a}$$

Using Eq. (7b) to cancel $\sigma_{zz}^{(i)}$ in Eq. (7d), one obtains the expression of σ_{zz}. Then, by plugging σ_{zz} and $u^{(i)}$ into Eq. (10), the out-of-plane equilibrium condition of the entire structure becomes

$$\overline{D}_m h_{in} w_{,xxxx} + D_m \left(w_{,xxxx}^{(n)} + w_{,xxxx}^{(1)} \right) -$$

$$G_t \left(u_{x,x}\big|_{z=\frac{h_{in}}{2}} - u_{x,x}\big|_{z=-\frac{h_{in}}{2}} + h_{in} w_{,xx} + \frac{t}{2}\left(u_{,zx}\big|_{z=\frac{h_{in}}{2}} + u_{,zx}\big|_{z=-\frac{h_{in}}{2}} + w_{,xx}\big|_{z=\frac{h_{in}}{2}} + w_{,xx}\big|_{z=-\frac{h_{in}}{2}} \right) \right) = f_z^{(1)} + f_z^{(n)} \tag{11b}$$

Meanwhile, plugging Eq. (11a) into Eq. (7c) and cancelling $u_x^{(i)}$ and its derivatives, the in-plane equilibrium condition of the 'surface' part becomes

$$\frac{E_{2D}}{1-\nu_p^2}\left(u_{,xx} + n_z \frac{t}{2}\left(u_{,zxx} + w_{,xxx}\right) - \frac{t}{4n^{(i)}}\left(w_{,xxx}^{(i)} + w_{,xxx}\right) \right) - G_t n^{(i)}\left(u_{,z} + w_{,x}\right) + f_x^{(i)} = 0 \tag{11c}$$

Similar to the classical beam theory(Gere and Timoshenko, 1995), we herein assume that a) no external shear force is applied on the
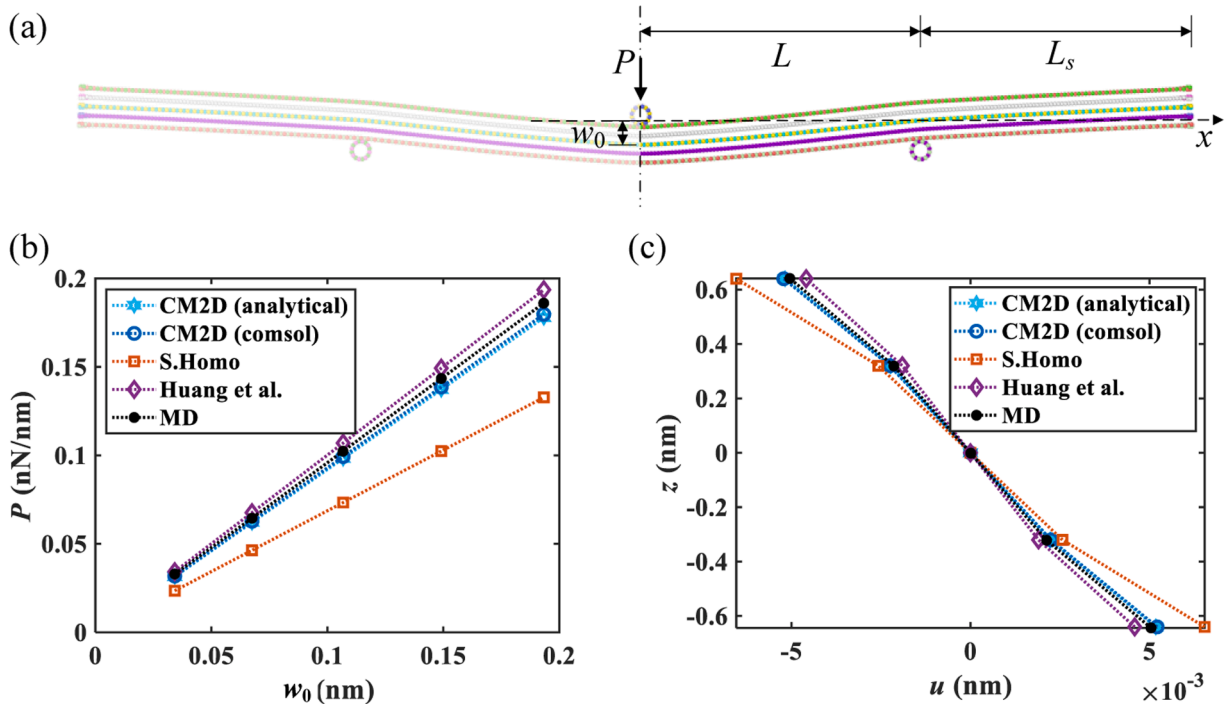

Fig. 3. (a) The atomic model of 3-point-bending h-BN beams in MD simulations. (b) The loads against middle point deflections of a 5-layer h-BN beam with L=10 nm and L_s=4.9 nm, and (c) its in-plane displacement distributions along z directionat $x/L = 0.3$ when w_0=0.19 nm. In (b) and (c), S.Homo represents the simple homogenization model.

outmost surfaces, i.e., $f_x^{(i)} = 0$. This leads to the anti-symmetric distribution of in-plane displacement over the thickness, i.e., $u(x, -z) = -u(x, z)$ and $u^{(1)} = -u^{(n)}$. b) The thickness does not change during deformation, i.e., $w(x, z) = w^{(i)}(x) = w(x)$. The external transverse load is denoted by $q = f_z^{(1)} + f_z^{(n)}$. Then, the in-plane equilibrium condition Eq. (6a) for 'bulk' part becomes

$$\frac{\overline{E}_{2D}}{1 - \nu_p^2} u_{,xx} + G_t u_{,zz} = 0 \tag{12a}$$

And the out-of-plane equilibrium condition for the entire structure can be obtained from Eq. (11b) as

$$n D_m w_{,xxxx} - G_t \left(2u_x \Big|_{z = \frac{h_{in}}{2}} + t u_{,zx} \Big|_{z = \frac{h_{in}}{2}} + (h_{in} + t) w_{,xx} \right) = q \tag{12b}$$

The equilibrium conditions for the 'surface' part are obtained from Eq. (11a) and Eq. (11c) as

$$u^{(i)} = u + n_z \frac{t}{2} u_{,z} \tag{12c}$$

$$\frac{E_{2D}}{1 - \nu_p^2} \left(u_{,xx} + n_z \frac{t}{2} u_{,zxx} \right) - G_t n_i \left(u_{,z} + w_{,x} \right) = 0 \tag{12d}$$

Eqs. (12) are the governing equations of the beam model within the CM2D framework. The displacement of the 'bulk' part is now partly coupled with the one of the 'surface' part, so we can solve the bulk displacement first, and then obtain their surface counterparts. Besides, in the second term of the right-hand side of Eq. (12c), $n_z u_{,z}$ is the outward derivative of the bulk displacement u. Therefore, the
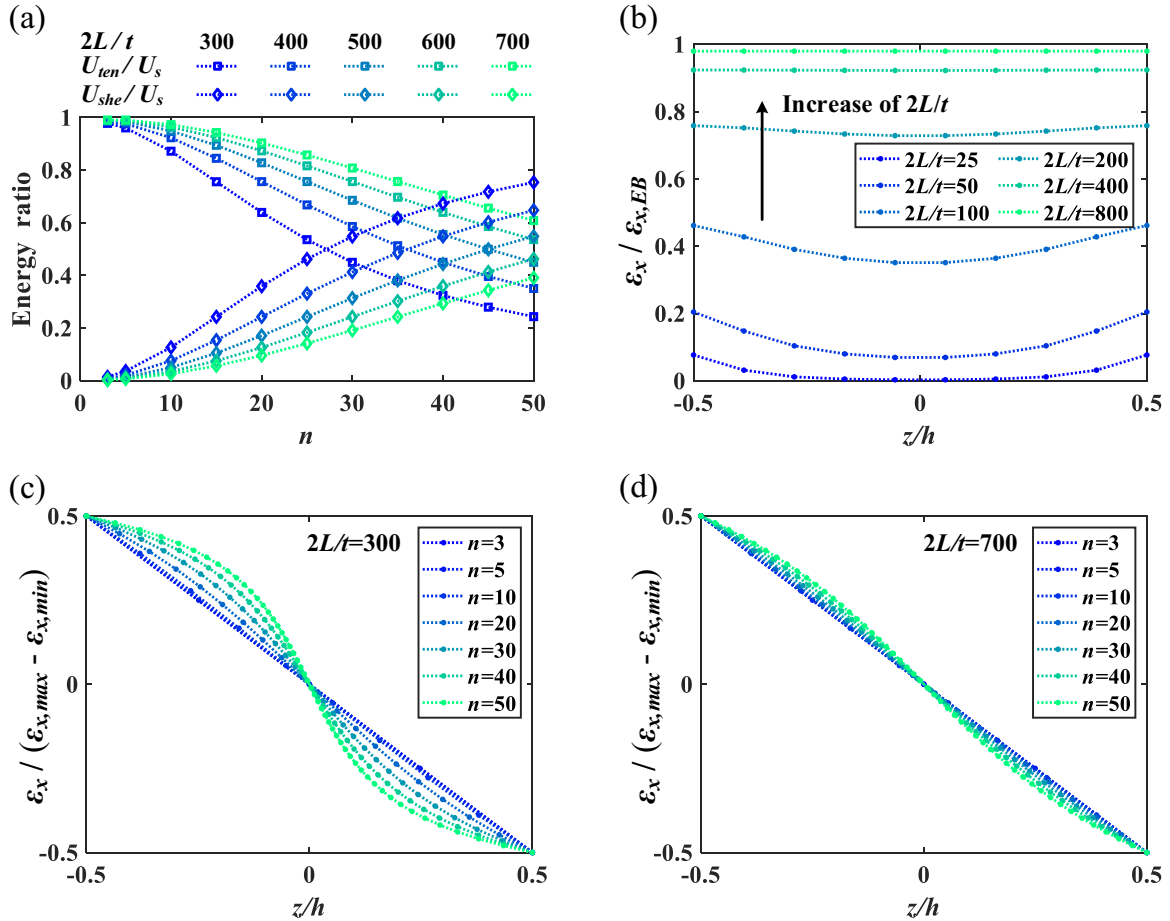

Fig. 4. (a) The ratios of intralayer tension energy U_{ten} and interlayer shear energy U_{she} to total strain energy U_s of h-BN beam with various n and L. (b) The normalized intralayer normal strain by its counterpart of the Euler-Bernoulli beam at $x/L = 0.3$ for a 10-layer h-BN beam with various L. The distribution of intralayer normal strain at $x/L = 0.3$ for (c) $2L/t = 300$ and (d) $2L/t = 700$ for h-BN beam with various n.

outmost layer displacements can be regarded as the linear extrapolation of the bulk ones $t/2$ away from the bulk boundaries.

3.1.2. Solution of the Beam model

The 3-point bending is a benchmark test for beams. In this sub-section, we will take a 3-point-bending beam as an example to discuss the bending behaviors of 2D material beams. As shown in Fig. 3a, suppose a 3-point-bending beam with its center located at (0,
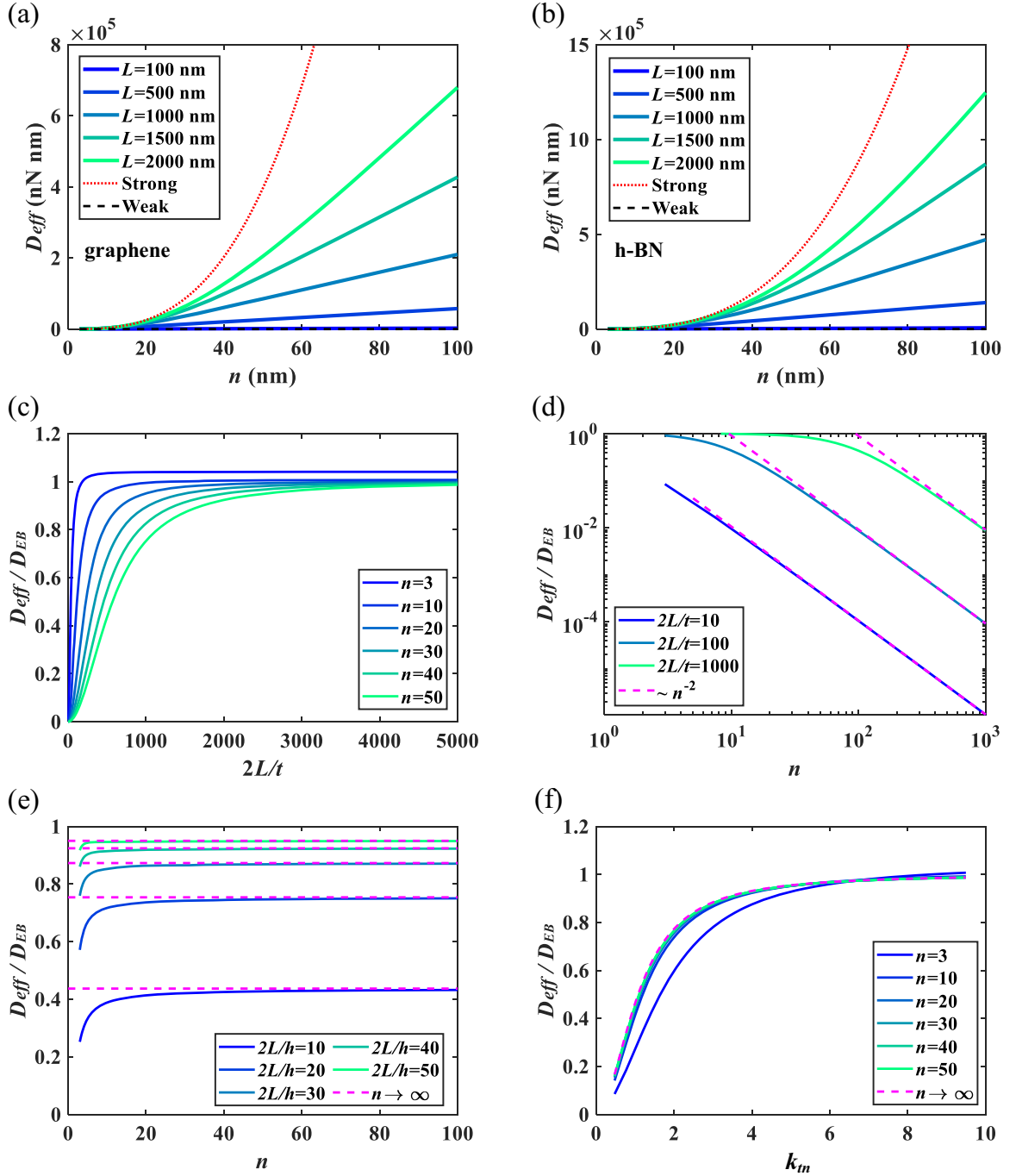
Fig. 5. The effective bending rigidity D_{eff} of (a) graphene and (b) h-BN beams as a function of layer number n parameterized by half length L, where the 'strong' and 'weak' correspond to the no-interlayer-shear-deformation limit and the no-interlayer-shear-resistance limit. The dimensionless effective bending rigidity D_{eff}/D_{EB} of h-BN beam as a function of (c) monolayer aspect ratio $2L/t$ parameterized by number of layers n, (d) number of layers n parameterized by monolayer aspect ratio $2L/t$, (e) number of layers n parameterized by overall aspect ratio $2L/h$, and (f) normalized tension-shear coefficient k_{tn} parameterized by number of layers n.

0). The undeformed middle line coincides with the x axis and is measured $2(L + L_s)$. The indenter is located at $x = 0$ and the two supporters at $x = \pm L$, respectively. Through obtaining the analytical solution (detailed in S6 in the Supplementrary Information), the tension-shear characteristic length $l_t = \sqrt{E_{2D}t/\left(1 - \nu_p^2\right)G_t}$ and bending-shear characteristic length $l_b = \sqrt{D_m/G_t t}$ are identified. Then, using the deformation length scale $2L$, we further define their dimensionless versions $k_t = 2L/l_t$ and $k_b = 2L/l_b$. Besides, the numerical solution employing the weak-form-PDE module of COMSOL is also obtained.

As shown in Fig. 3b and c, both our analytical and numerical results match fairly well with MD simulations (see Fig. 3a and S1 of the Supplementary Information for detail). For comparison, we also construct a simple homogenization model (S.Homo.) without considering the surface layer effect of 2D materials. Its results are too soft, because the concentrated 2D material sheets at the outmost layers are re-distributed inward, impairing the total bending rigidity. The continuous beam solution proposed by Huang et al.(Huang et al., 2023) is also close to the MD simulations, though their results are a little bit stiffer. This is because their solution actually corresponds to a beam model similar to ours, except that the two outmost half interlayers are also stiffened using the bulk materials.

Furthermore, as another validation of our model, the stepwise bending experiments were also carried out, where multilayer graphene was placed on the graphene steps. Under the competition between the strain energy and interfacial adhesion energy, the multilayer graphene can reach an equilibrium configuration (detailed in S5 of the Supplementary Information). As shown in Fig.S6, the prediction of CM2D matches the experimental measurements well.

3.1.3. Deformation mode of 2D material beams

The bending deformation mode of a 2D material beam is controlled by the competition between the intralayer tensile and interlayer shear deformation modes. The increase in n can suppress the intralayer deformation mode, while encourage the interlayer shear deformation mode. As a result, the percentage of intralayer tension strain energy decreases, while that of interlayer shear strain energy increases (see Fig. 4a). This is because when n is small, the demand for interlayer shear stress to transfer loads, thereby maintaining the intralayer deformation and the planar cross-section, is relatively small. Thus, the deformed cross-section doesn't stray away too much from the planar shape and the distribution of normal strain on a cross-section remains linear (see Fig. 4c and d). However, as n increases, maintaining the intralayer deformation and the planar cross-section becomes so energetically costly that interlayer shear deformation manifests itself. The deformed cross-section tends to be curvy and the distribution of normal strain becomes nonlinear.

On the other hand, intralayer deformation modes tend to prevail in slender beams. The decrease in tension strain energy ratio U_{ten}/U_s and the increase in shear strain energy ratio U_{she}/U_s as n increases are significantly slowed down (see Fig. 4a). Based on Eq. (6a), the increase in intralayer tension stress can be expressed as $d\sigma_x = -\left(d\tau_{zx}/dz\right)dx$, which suggests that the intralayer tension stress picks up its value through the accumulation of adjacent interlayer shear stress differences. For stubby beams, the length for intralayer stress to accumulate is insufficient. Therefore, the intralayer stress or strain level is low compared to that of the Euler-Bernoulli beam (EB), while the interlayer shear deformation mode is encouraged to cope with the external loads. The deformed cross-section becomes curvy, and the distribution of normal stress or strain becomes nonlinear upon a slight increase in n (Fig. 4c). By contrast, for slender beams, the intralayer tension stress or strain can be fully developed and even reaches the EB level through a quite small region, leaving most parts of the beam possessing an intralayer tension stress or strain level extremely close to the EB. As shown by Fig. 4b, the intralayer strain approaches that of EB upon increasing L. In this case, the deformed cross-section deviates slightly from the planar assumption, and the distribution of normal stress or strain is relatively close to a planar pattern, even though n increases (Fig. 4d).

3.1.4. Effective Bending Rigidity of 2D Material Beams

Bending rigidity is an important parameter of 2D material beams, which is different from the one of a single EB or a stack of EBs because of the finite interlayer shear resistance(Chen et al., 2015; Wang et al., 2019; Han et al., 2019). Here, we will discuss the bending rigidity of h-BN beams based on our CM2D beam model.

According to the 3-point-bending of the EB beam and Eq. (S6.3c), the effective bending rigidity is expressed as

$$D_{eff} = \frac{PL^3}{6w_0} = \frac{G_t L^2 t}{24\sum_{k=1}^{\infty}\frac{1}{\Lambda_k}} \tag{13}$$

For a specific material, Λ_k only depends on the deformation length scale $2L$ and the number of layers n (see Eq. (S6) in the Supplementary Information), and so does D_{eff}. The dependence of D_{eff} of two popular 2D materials, graphene and h-BN, are shown in Fig. 5a and 5b, respectively (see Table.S1 in the Supplementary Information for material parameters). The EB bending rigidity of 2D materials is(Chen et al., 2023; Koskinen and Kit, 2010)

$$D_{EB} = \frac{n(n^2 - 1)E_{2D}t^2}{12\left(1 - \nu_p^2\right)} + nD_m \tag{14}$$

Then, normalize the effective bending rigidity by D_{EB}, and the resultant dimensionless effective bending rigidity becomes

$$\overline{D}_{eff} = \frac{D_{eff}}{D_{EB}} = \frac{1}{8n\left(\frac{(n^2-1)}{k_t^2} + \frac{12}{k_b^2}\right)\sum_{k=1}^{\infty}\frac{1}{\Lambda_k}} \tag{15}$$

which explicitly depends on dimensionless parameters k_t, k_b and n. For now, since we are focused on a specific material, i.e., h-BN, the characteristic lengths, l_t and l_b, are settled. Only the effects of geometric parameters L and n are discussed.

As shown in Fig. 5c, the dimensionless effective bending rigidity increases with L. As $L \to \infty$, $\overline{D}_{eff}$ approaches its limit value, i.e.,

$$\lim_{L\to\infty}\overline{D}_{eff} = \frac{12nl_b^2 + (n^3 - 2)l_t^2}{12nl_b^2 + (n^3 - n)l_t^2} \tag{16}$$

which approaches to 1 as n increases. This is because the intralayer deformation mode gradually dominates the bending deformation as the beam becomes increasingly slender. Therefore, the effective bending rigidity could be slightly larger than its EB counterpart, if n is quite small yet L is large enough. Similar phenomenon has also been reported by Huang et al. (Huang et al., 2023) By contrast, the increase in n will reduce $\overline{D}_{eff}$, and even drive $\overline{D}_{eff}$ to decay proportionally with n^{-2} when n is large enough (see Fig. 5d). More specifically,

$$\overline{D}_{eff} \sim \frac{k_t^2}{1 - \frac{2}{k_b}\tanh\left(\frac{k_b}{2}\right)}\frac{1}{n^2} \tag{17}$$

This suggests that the effective bending rigidity of 2D material beam D_{eff}, scales with n when n is large, given that D_{EB} scales with n^3.

If the overall aspect ratio $A = 2L/h = 2L/(n-1)t$ or the normalized tension-shear coefficient $k_{tn} = k_t/(n-1)$ is fixed so that L can vary nearly proportionally to n, $\overline{D}_{eff}$ will increase and approach a constant as n increases (see Fig. 5e). The limit value depends on A or k_{th} in such way that

$$\left(\lim_{n\to\infty}\overline{D}_{eff}\right)_{\text{A or } k_{tn}} = \frac{1}{8l_t^3\sum_{k=1}^{\infty}\frac{1}{\omega_k t^2 A^2\left(l_t\omega_k - 2t\text{Atanh}\left(\frac{l_t\omega_k}{2tA}\right)\right)}} = \frac{1}{8\sum_{k=1}^{\infty}\frac{1}{k_{tn}^2\omega_k\left(\omega_k - 2k_{tn}\tanh\frac{\omega_k}{2k_{tn}}\right)}} \tag{18}$$

which increases monotonically and approaches 1 as A or k_{tn} increases. More interestingly, Eq. (18) describes a master curve, to which the $\overline{D}_{eff}$ v.s. A curve or $\overline{D}_{eff}$ v.s. k_{th} curve will quickly collapse as n increases (see Fig. 5f). In other words, it won't bring too much error to regard $\overline{D}_{eff}$ as a function independent of n (depicted by Eq. (18)), if n is not so small, e.g., $n > 10$.

3.2. Plate model of 2D materials

3.2.1. Plate model within the CM2D framework

Different from one-dimensional beam model, the plate model is used for 2D bending deformations. Similarly, two assumptions are adapted: a) no shear on the surface and b) no thickness change during the deformation. Then, the governing equations of the plate model can be obtained through similar operations in Section 3.1. For the 'bulk' part, we have

$$\frac{1}{2}\frac{\overline{E}_{2D}}{1-\nu_p}u_{\beta,\alpha\beta} + \frac{1}{2}\frac{\overline{E}_{2D}}{1+\nu_p}u_{\alpha,\beta\beta} + G_t u_{\alpha,33} = 0 \tag{19a}$$

$$nD_m w_{,\alpha\alpha\beta\beta} - G_t\left(2u_{\alpha,\alpha}\Big|_{z=\frac{h_{in}}{2}} + tu_{\alpha,\alpha3}\Big|_{z=\frac{h_{in}}{2}} + (h_{in} + t)w_{,\alpha\alpha}\right) = q \tag{19b}$$

and for the 'surface' region, we can obtain

$$\frac{1}{2}\frac{E_{2D}}{1-\nu_p}\left(u_{\beta,\alpha\beta} + \frac{t}{2}u_{\beta,3\alpha\beta}n_3\right) + \frac{1}{2}\frac{E_{2D}}{1+\nu_p}\left(u_{\alpha,\beta\beta} + \frac{t}{2}u_{\alpha,3\beta\beta}n_3\right) - n_i G_t(u_{\alpha,3} + w_{,\alpha}) = 0 \tag{19c}$$

$$u_\alpha^{(i)} = u_\alpha + \frac{t}{2}u_{\alpha,3}n_3 \tag{19d}$$

Moreover, the axisymmetric condition is ubiquitous in nano-experiments, which can be used to simplify the governing equations, i. e., Eq. (19), into

$$\frac{\overline{E}_{2D}}{1-\nu_p^2}\left(\frac{\partial^2 u_r}{\partial r^2} + \frac{1}{r}\frac{\partial u_r}{\partial r} - \frac{u_r}{r^2}\right) + G_t\frac{\partial^2 u_r}{\partial z^2} = 0 \tag{20a}$$

$$nD_m\nabla^2\nabla^2 w - G_t\left(2\left(\frac{\partial u_r}{\partial r} + \frac{u_r}{r}\right)\Big|_{z=\frac{h_{in}}{2}} + t\frac{\partial}{\partial z}\left(\frac{\partial u_r}{\partial r} + \frac{u_r}{r}\right)\Big|_{z=\frac{h_{in}}{2}} + (h_{in} + t)\nabla^2 w\right) = q \tag{20b}$$

for the 'bulk' part, and

$$\frac{E_{2D}}{1-\nu_p^2}\left(\frac{\partial}{\partial r}\left(\frac{\partial u_r}{\partial r}+\frac{u_r}{r}\right)+\frac{t}{2}\frac{\partial}{\partial z}\left(\frac{\partial}{\partial r}\left(\frac{\partial u_r}{\partial r}+\frac{u_r}{r}\right)\right)n_z\right)-n_iG_t\left(\frac{\partial u_r}{\partial z}+\frac{dw}{dr}\right)=0 \tag{20c}$$

$$u_r^{(i)}=u_r+\frac{t}{2}\frac{\partial u_r}{\partial z}n_z \tag{20d}$$

for the 'surface' part. $\nabla^2=\frac{\partial^2}{\partial r^2}+\frac{1}{r}\frac{\partial}{\partial r}$ is the 2D axisymmetric Laplace operator and the subscript 'r' in Eq. (20) denotes the radial component. The dummy index convention is not applied to Eq. (20). Similarly, we may solve the bulk displacement first, and then obtain their surface counterparts. The outmost layer displacements can be regarded as the linear extrapolation of the bulk ones $t/2$ away from the bulk boundaries.

3.2.2. Solution of the Plate model

Bulging a bubble has been used for measuring important parameters for 2D materials, such as interlayer shearing strength, intralayer stiffness and bending rigidity(Wang et al., 2017, 2019; Yue et al., 2012; Li et al., 2024). It is even developed to uniaxially stretch the specimens by employing a rectangular-shaped bubble, making it capable of performing the most fundamental mechanical test(Cui et al., 2023). In this subsection, we take the axisymmetric bubble as an example to explain the numerically solving method.

The bubble solution is obtained by employing the weak-form-PDE module of COMSOL based on the governing equations Eqs. (20). Denote the radius of the bulged area by R. Considering the axisymmetry, the bulk in-plane displacement $u_r(r,z)$ is defined on a 2D domain $[0,R]\times[-h_{in}/2,h_{in}/2]$, while the out-of-plane deflection $w(r)$ and the surface in-plane displacement $u_r^{(i)}(r)$ are defined in an interval $[0,R]$. Note that we treat $u_r(r,z)$ and $w(r)$ as two general mathematical functions, so they don't need to be defined on the same domain. Besides, $w(r)$ needs to be mapped to the 2D domain and $u_r(r,\pm h_{in}/2)$ to the interval, so that all the strain components given by Eq. (1) and (2) can be properly evaluated. The fixed boundary conditions are expressed as $u_r(R,z)=0$, $u_r^{(i)}(R)=0$, $w(R)=0$, $\partial w(R)/\partial r=0$. A uniformly distributed load is prescribed to $w(r)$ field as a virtual work term. As shown in Fig. 6, the solution of the CM2D plate model matches fairly well with MD simulations, while the solution of simple homogenization model without surface layer effect (S.Homo.) predicts a much more softened displacement as expected. The MD simulation is detailed in S1 of the Supplementary Information.
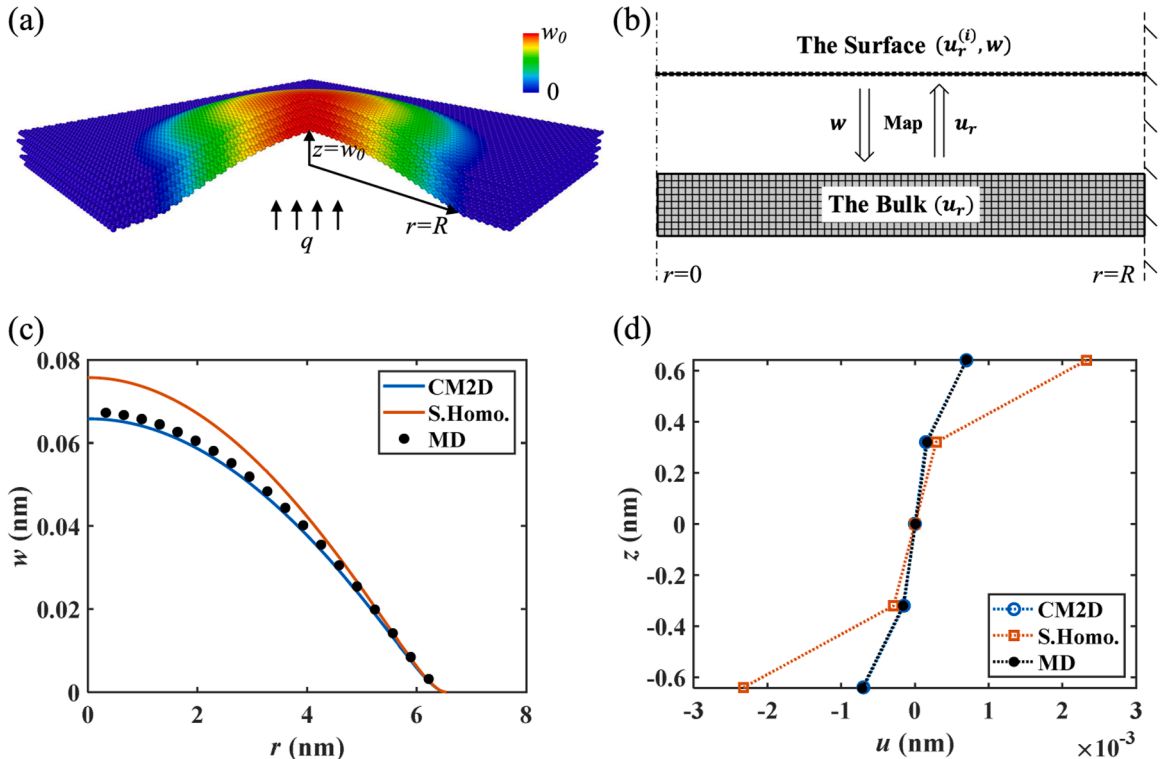
Fig. 6. (a) Atomic model of bulged circular 5-layer h-BN bubble. (b) Illustration of COMSOL model employing weak-form-PDE module for numerical solution. (c) Deflection curves and (d) in-plane displacement distribution along the z direction at $r/R=0.3$ of a 5-layer h-BN bubble with $R=6.546$ nm and $q=0.0593$ GPa.

It is worth mentioning that the numerical method for bubble can be easily adapted for rectangular plates. Since the axisymmetry is lost in rectangular plates, the definition domains of bulk in-plane displacements $u_\alpha(x_1, x_2, x_3)$ are extended to 3D, and the definition domains of the rest of the displacement components are extended to 2D.

3.2.3. Bending deformation mode of 2D material plate

The bending deformation mode of 2D material plates is also controlled by the competition between the intralayer deformation and interlayer shear deformation modes. On the one hand, as the 2D material sheets are piled up, the demand for interlayer shear stress to transfer loads between layers and to maintain planar cross-section during bending increases. This will gradually make the interlayer shear deformation mode prevail in the strain energy sense. As shown in Fig. 7a, the percentage of shear strain energy reaches and surpasses that of intralayer strain energy with increased n. Besides, the section may even be unable to maintain planar. As shown in Fig. 7c and d, the distribution of intralayer normal strain at a cross-section becomes increasingly curvy with n growing. Therefore, the increase in n tends to encourage the interlayer shear deformation and drive the deformed section curvy.

On the other hand, with the increase in R, the intralayer tension stress can accumulate more easily so that the steep decreasing trend of its energy percentage is slowed down (Fig. 7a) and its gap with the ideal no-interlayer-shear scenario, i.e., the Kirchhoff plate, is narrowed down even to neglectable extent. As shown in Fig. 7b, the intralayer normal strain gradually catches up with that of Kirchhoff plates. Furthermore, the curvy cross-section tends to be straightened. The distribution of cross-section normal strain becomes linearized as R increases (Fig. 7c and d). At this time, the intralayer deformation mode becomes dominating.

Given that the uniformly loaded axisymmetric plate is a quasi-one-dimensional problem, its bending behavior is similar to that of a beam. Nevertheless, it's important to note that the CM2D plate model and the CM2D beam model are fundamentally different. In fact, our proposed CM2D plate model (Eqs. (19)) can handle general plate-like deformation modes. For instance, in the case of a rectangular plate (the axisymmetry is broken), the results (see Fig.S2) indicate that the deformed normal lines, initially perpendicular to the middle plane, become 3D curves in general and vary with coordinates, which are beyond the ability of a beam theory. A more detailed discussion on the deformation modes of the plate within the CM2D framework will be addressed in our future work.
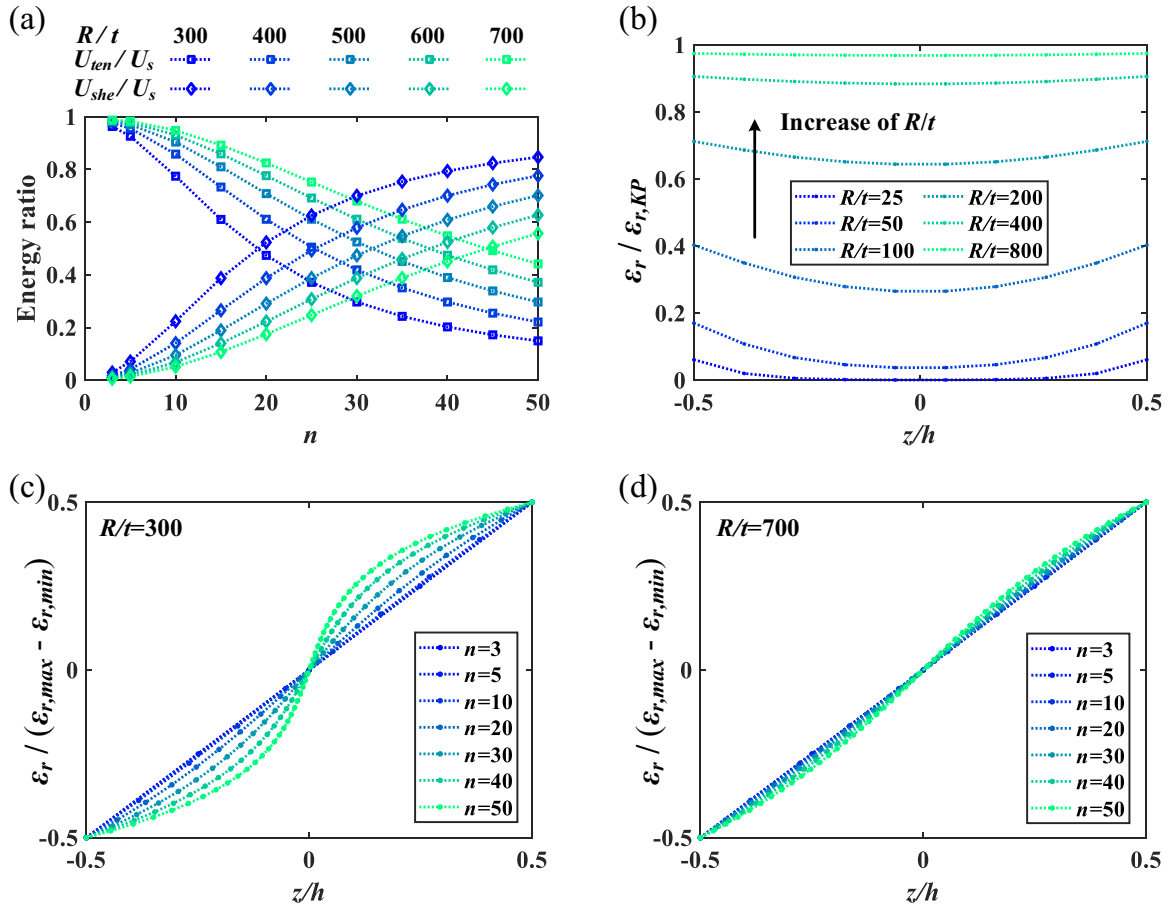

Fig. 7. (a) The ratios of intralayer tension energy U_{ten} and interlayer shear energy U_{she} of h-BN plate to its total strain energy U_s with various n and R. (b) The normalized intralayer normal strain of a 10-layer h-BN plate by its counterpart of Kirchhoff plate at $r/R = 0.3$ with various R. The intralayer normal strain distribution at $r/R = 0.3$ for (c) $R/t = 300$ and (d) $R/t = 700$.

3.2.4. *Effective bending rigidity of 2D material plate*

As the critical parameter of 2D material plates, its bending rigidity has drawn a lot of attention(Wang et al., 2019; Ma et al., 2022). In this subsection, we will discuss the bending rigidity of h-BN plates based on our CM2D plate model. According to the solution of the Kirchhoff plate(Timoshenko and Woinowsky-Krieger, 1976), the effective bending rigidity of a plate can be expressed in terms of the uniform loads q and the center deflection w_0, as
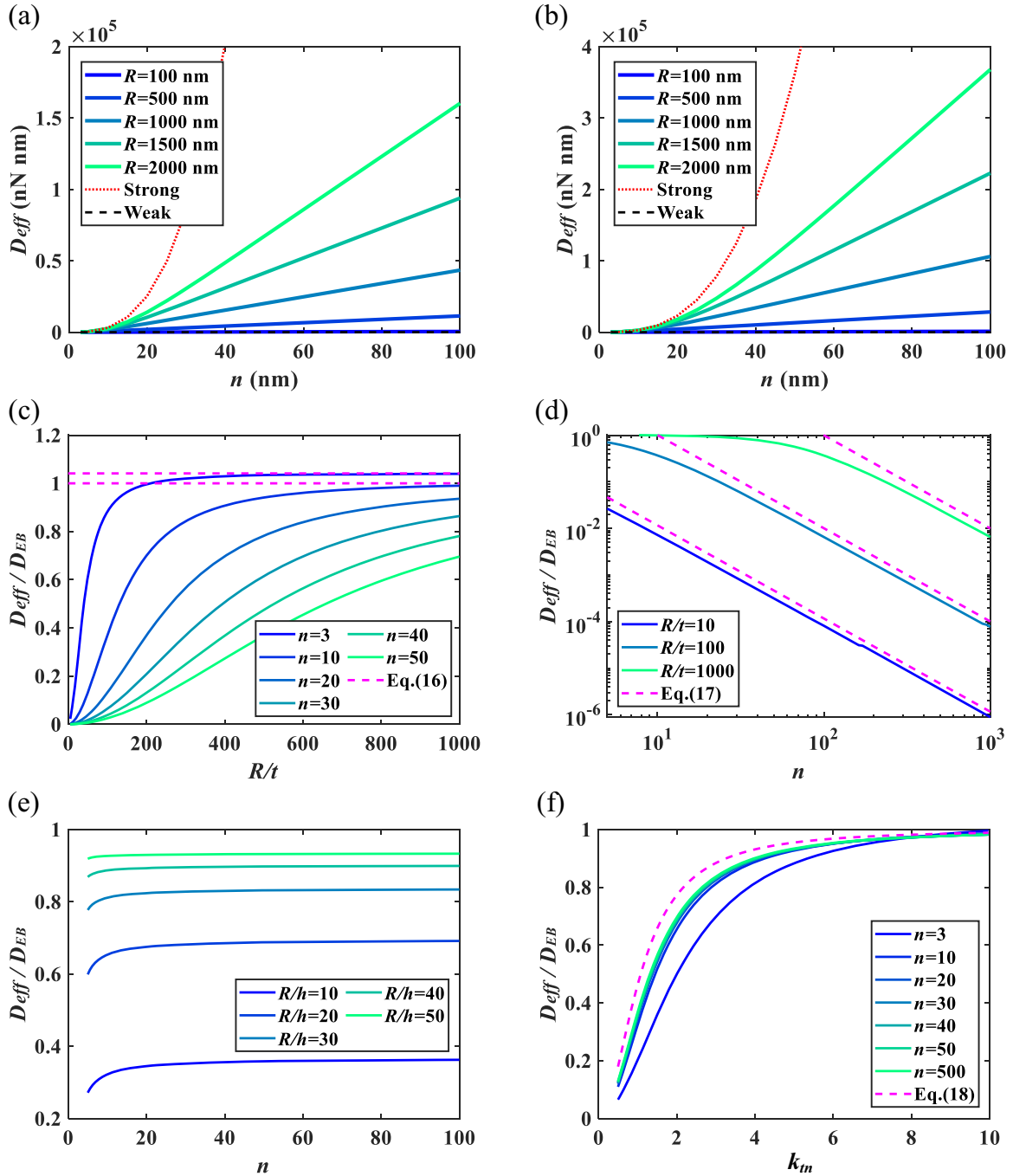
Fig. 8. The effective bending rigidity D_{eff} of (a) graphene and (b) h-BN plates as a function of layer number n parameterized by half length L, where the 'strong' and 'weak' correspond to the no-interlayer-shear-deformation limit and the no-interlayer-shear-resistance limit. The dimensionless effective bending rigidity D_{eff}/D_{EB} of h-BN plate against (c) monolayer aspect ratio R/t parameterized by number of layers n, against number of layers n parameterized by (d) monolayer aspect ratio R/t and (e) overall aspect ratio R/h, and against (f) normalized tension-shear coefficient k_{tn} parameterized by number of layers n.

$$D_{eff} = \frac{qR^4}{64w_0} \tag{21}$$

The dependence of D_{eff} of two popular 2D materials, graphene and h-BN, are shown in Fig. 8a and 8b, respectively (see Table.S1 in the Supplementary Information for material parameters).

Similarly, we will discuss the dimensionless effective bending rigidity $\overline{D}_{eff}$ defined by Eq. (15), where the bending rigidity of Kirchhoff plate D_{EB} is still evaluated through Eq. (14).

To determine the factors that may influence $\overline{D}_{eff}$, we denote the dimensionless coordinates and displacement field as $\bar{r} = r/R$, $\bar{z} = z/t$, $\overline{w} = w/w_0$, $\overline{u}_{\bar{r}} = u_r/w_0$, $\overline{u}_{\bar{r}}^{(i)} = u_r^{(i)}/w_0$, and obtain the dimensionless form of the governing equations Eqs. (20) as

$$\frac{1}{k_t^2} \frac{\partial}{\partial \bar{r}} \left(\frac{\partial}{\partial \bar{r}} + \frac{1}{\bar{r}} \right) \overline{u}_r + \frac{\partial^2 \overline{u}_r}{\partial \bar{z}^2} = 0 \tag{22a}$$

$$\frac{n}{k_b^2} \overline{\nabla}^2 \overline{\nabla}^2 \overline{w} - \left(2\alpha \left(\frac{\partial \overline{u}_r}{\partial \bar{r}} + \frac{\overline{u}_r}{\bar{r}} \right) \bigg|_{\bar{z}=\frac{n-2}{2}} + \alpha \frac{\partial}{\partial \bar{z}} \left(\frac{\partial \overline{u}_r}{\partial \bar{r}} + \frac{\overline{u}_r}{\bar{r}} \right) \bigg|_{\bar{z}=\frac{n-2}{2}} + (n-1)\overline{\nabla}^2 \overline{w} \right) = \frac{qR^2}{G_t t w_0} \tag{22b}$$

for the bulk and
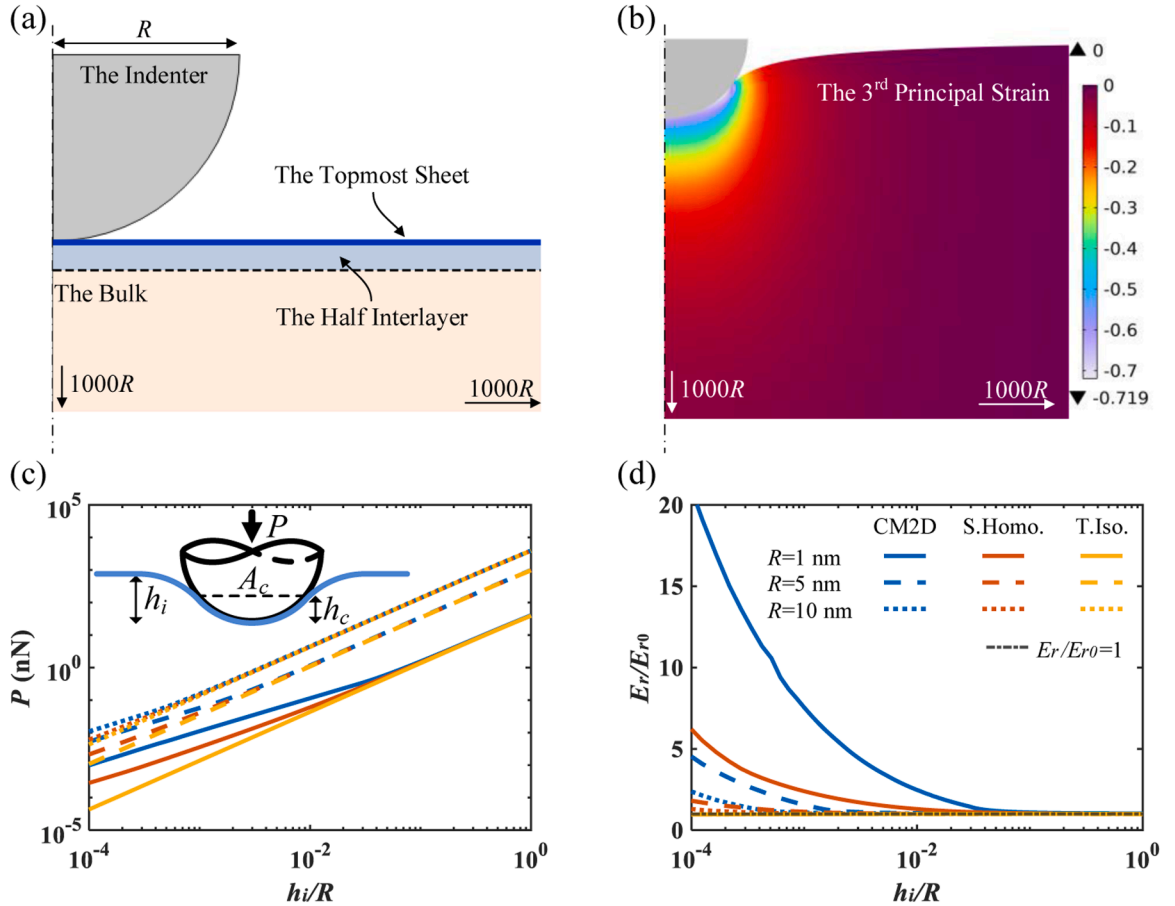
Fig. 9. (a) Illustration of the numerical model using Solid Mechanics module as implemented in COMSOL. (b) Zoomed-in view near the indenter tip (*R*=1 nm) of the third principal strain distribution on the deformed configuration during indentation into h-BN materials. (c) The log-log plot of the indentation force-normalized depth curve and (d) the semi-log plot of the inferred normalized reduced modulus-depth curve with indenter radius *R*=1 nm, 5 nm, 10 nm and various material models. In (c) and (d), T.Iso. represents the classical transversely isotropic elasticity model, and S.Homo represents the simple homogenization model as mentioned in Section 3.1.2. The inset in (c) gives an illustration of an indenter pressed into a specimen.

$$\frac{1}{k_t^2}\left(\frac{\partial}{\partial \overline{r}}\left(\frac{\partial \overline{u}_r}{\partial \overline{r}} + \frac{\overline{u}_r}{\overline{r}}\right) + \frac{1}{2}\frac{\partial}{\partial \overline{z}}\left(\frac{\partial}{\partial \overline{r}}\left(\frac{\partial \overline{u}_r}{\partial \overline{r}} + \frac{\overline{u}_r}{\overline{r}}\right)\right)n_z\right) - n_i\left(\frac{\partial \overline{u}_r}{\partial \overline{z}} + \frac{1}{\alpha}\frac{\mathrm{d}\overline{w}}{\mathrm{d}\overline{r}}\right) = 0 \tag{22c}$$

$$\overline{u}_r^{(i)} = \overline{u}_r + \frac{1}{2}\frac{\partial \overline{u}_r}{\partial \overline{z}}n_z \tag{22d}$$

for the surface, where $\overline{\nabla}^2 = \frac{\partial^2}{\partial \overline{r}^2} + \frac{1}{\overline{r}}\frac{\partial}{\partial \overline{r}}$. The dimensionless parameters in Eqs. (22) turn out to be similar to their beam counterparts, except that the deformation scale $2L$ in the beam is replaced here by R in the plate, i.e., $k_t = R/l_t$, $k_b = R/l_b$, $\alpha = R/t$. This suggests that the dimensionless effective bending rigidity also depends on k_t, k_b and n.

Indeed, the dimensionless effective bending rigidity of 2D material plate behaves similarly to its beam counterpart with various geometric parameters, R and n, but not exactly the same. As shown in Fig. 8a, $\overline{D}_{eff}$ increases and approach a limit that also can be described by Eq. (16), as the geometric scale of the plate R increases. Likewise, the effective bending rigidity of 2D material plate can be slightly larger than the Kirchhoff plate as long as R is large enough and n is quite small. $\overline{D}_{eff}$ still decreases as n increases, and approximately proportionally to n^{-2} when n is large enough. This also suggests that D_{eff} of 2D material plate scale with n, as n is large enough. However, the decaying coefficient is smaller than that given by Eq. (17), as shown in Fig. 8b, where the solid lines shift slightly downward from the dashed lines. When the overall aspect ratio A $= R/h$ or the normalized tension-shear coefficient k_{tn} is fixed, $\overline{D}_{eff}$ still increases and quickly approaches a limit with increasing n (see Fig. 8c). This limit is dominated almost only by k_{tn} when n is not too small, as shown in Fig. 8d. However, the master curve of beam given by Eq. (18), represented by the magenta dash line, can no longer depict this limit well.

In addition, we further validate the CM2D model using the results of bubble experiments(Wang et al., 2019). The employed material parameters are list in Table.S1 and the geometric parameters from experiments(Wang et al., 2019) are adopted. As shown in Fig. S7, the predictions of effective bending rigidity through CM2D plate model and Eq. (21) are in good agreement with the results obtained in experiments (Wang et al., 2019). All the results are always bounded by the two theoretical limits, i.e., the strong limit (red dot line) corresponding to no interlayer shear deformation and the weak limit (black dash line) corresponding to no interlayer shear resistance, consistent with previous works(Chen et al., 2022; Han et al., 2019; Huang et al., 2023; Ma et al., 2022).

3.3. Indentation of 2D materials

Indentation has become a powerful tool for material testing(Oliver and Pharr, 2010; Zhang and Needleman, 2021; Yuan et al., 2023), among which depth sensing indentation technique can infer elastic modulus merely from the indentation load-depth data and the shape function of the indenter(Oliver and Pharr, 1992). The extremely sharp tip of atomic force microscope, usually used as the indenter in a nano-indentation test, features high curvature and forces the specimen to conform to its shape near the contact surface, when pressed into a 2D material perpendicularly to its sheets. As a result, the topmost and following 2D material sheets need to bear severe bending deformation. In this process, the surface layer effect and monolayer bending effect may play an important role, even though the material volume may consist of countless 2D material sheets. In this subsection, we will study the indentation of a rigid spherical indenter pressed into 2D material half-space within the proposed CM2D framework.

For an arbitrary smooth axisymmetric indenter pressed into a specimen (illustrated by the inset in Fig. 9c), the reduced modulus can be expressed as(Pharr et al., 1992; Sneddon, 1965)

$$E_r = \frac{\sqrt{\pi}}{2}\frac{S}{\sqrt{A_c}} \tag{23}$$

where, the unloading rigidity $S = \mathrm{d}P/\mathrm{d}h_i$ is the derivative of indentation force P with respect to indentation depth h_i. A_c is the projection area of contact surface, aka the shape function, depending on the distance between the contact edge and the indenter tip h_c, which can be inferred also through the force-displacement data as $h_c = h_i - \epsilon P/S$ (Oliver and Pharr, 1992). For a rigid spherical indenter, $A_c = 2\pi R h_c - \pi h_c^2$, and ϵ can approximately take the value of paraboloid indenter as 0.75. For classical materials, the reduced modulus E_r only depends on the material parameters. For example, the reduced modulus of transversely isotropic materials indented perpendicular to its isotropic plane by a rigid indenter is(Delafargue and Ulm, 2004; Lamuta, 2019)

$$E_{r0} = \frac{2}{\sqrt{\frac{C_{11}}{C_{11}C_{33}-C_{13}^2}\left(\frac{1}{C_{44}} + \frac{2}{\sqrt{C_{11}C_{33}+C_{13}}}\right)}} \tag{24}$$

where C_{ij} is the element of stiffness matrix. Therefore, the reduced modulus is actually a comprehensive elastic parameter reflected by the indentation test, which bridges the direct experiment measurements to the intrinsic elastic parameters of materials.

3.3.1. 3D axisymmetric model within the CM2D framework

Some problems, such as indention on half-space by axisymmetric indenters perpendicular to the isotropic plane, possess axisymmetry. Thus, the governing equations can be simplified accordingly. To achieve this, we first re-express Eqs. (1)~(4) and (6)~ (9) under a cylindrical coordinate system. Then, we leverage the axisymmetry of the deformation field, i.e., the angular component of

displacement remains 0 during deformation. As a result, we can obtain the governing equations, for the 'bulk' part as

$$\frac{\overline{E}_{2D}}{1-\nu_p^2}\frac{\partial}{\partial r}\left(\frac{\partial}{\partial r}+\frac{1}{r}\right)u_r + G_t\frac{\partial}{\partial z}\left(\frac{\partial u_r}{\partial z}+\frac{\partial w}{\partial r}\right)+f_r = 0 \tag{25a}$$

$$G_t\left(\left(\frac{\partial}{\partial r}+\frac{1}{r}\right)\frac{\partial u_r}{\partial z}+\nabla_{2D}^2 w\right)+E_t\frac{\partial^2 w}{\partial z^2}-\overline{D}_m\nabla_{2D}^2\nabla_{2D}^2 w + f_z = 0 \tag{25b}$$

and for the 'surface' part as

$$G_t\left(\left(\frac{\partial u_r}{\partial z}+\frac{\partial w}{\partial r}\right)n_z - \left(\frac{u_r^{(i)}-u_r}{t/2}+n^{(i)}\frac{1}{2}\left(\frac{\partial w^{(i)}}{\partial r}+\frac{\partial w}{\partial r}\right)\right)\right)\delta u_r = 0 \tag{25c}$$

$$\left(E_t\frac{\partial w}{\partial z}n_z - \frac{1}{4}G_t t\left(\frac{\partial}{\partial r}+\frac{1}{r}\right)\left(\frac{u_r^{(i)}-u_r}{t/2}n^{(i)}+\frac{1}{2}\left(\frac{\partial w^{(i)}}{\partial r}+\frac{\partial w}{\partial r}\right)\right)-\frac{2}{t}E_t\left(w^{(i)}-w\right)\right)\delta w = 0 \tag{25d}$$

$$\left(\frac{E_{2D}}{1-\nu_p^2}\frac{\partial}{\partial r}\left(\frac{\partial}{\partial r}+\frac{1}{r}\right)u_r^{(i)}-G_t\left(\frac{u_r^{(i)}-u_r}{t/2}+n^{(i)}\frac{1}{2}\left(\frac{\partial w^{(i)}}{\partial r}+\frac{\partial w}{\partial r}\right)\right)+f_r^{(i)}\right)\delta u_r^{(i)} = 0 \tag{25e}$$

$$\left(G_t\left(n^{(i)}\frac{1}{2}\left(\frac{\partial}{\partial r}+\frac{1}{r}\right)\left(u_r^{(i)}-u_r\right)+\frac{t}{8}\nabla_{2D}^2\left(w^{(i)}+w\right)\right)-E_t\frac{w^{(i)}-w}{t/2}-D_m\nabla_{2D}^2\nabla_{2D}^2 w^{(i)}+f_z^{(i)}\right)\delta w^{(i)} = 0 \tag{25f}$$

where $\nabla_{2D}^2 = \frac{\partial^2}{\partial r^2}+\frac{1}{r}\frac{\partial}{\partial r}$ is the 2D axisymmetric Laplace operator defined on isotropic plane. Unlike axisymmetric plate model Eqs. (20) which assumes the undeformed thickness, Eqs. (25) take the deformation of thickness into consideration, i.e., w doesn't equal $w^{(i)}$ in general. The analytical solution can be subtle, necessitating the use of numerical methods.

3.3.2. Solution of indentation

To leverage the optimized code of COMSOL for solving contact problems, its Solid Mechanics module is adapted to approximate Eq. (25). The problem is solved in a 2D domain, thanks to the axisymmetry. As shown in Fig. 9a, the indenter is modeled by a quarter of a rigid circle with radius R. The 2D material specimen is divided into three parts according to the CM2D model (Fig. 2a). The stiffness parameters E_{2D}, ν_p, D_m, D_g of a monolayer 2D material sheet are assigned to the top boundary through 'weak contribution' to model the topmost sheet. Below it is the half layer of interlayer media with transverse Young's modulus E_t and transverse shear modulus G_t. Note that an in-plane Young's modulus E_{in}, three orders of magnitude smaller than E_t, is also assigned to the half layer of interlayer media, so that its stiffness matrix is not singular and meanwhile the disturbance caused by this operation can be neglected. It has been validated that making E_{in} even smaller won't cause appreciable difference. The following 'bulk' part is also basically transversely isotropic with parameters described in Section 2, except that the bending modulus $\overline{D}_m$ and Gaussian bending modulus $\overline{D}_g$ are assigned to it by 'weak contribution'. The specimen spans $1000R$ in both width and height. It should be noted that the specimen size is sufficiently large to model the material half-space, since a larger size won't make any appreciable difference. The augmented Lagrangian method is employed to solve the frictionless hard contact between the indenter and the specimen. Note that the adhesion between the indenter and 2D materials is not considered at present(Li et al., 2016), which will be further explored in our future work. Besides, the normal displacement of the bottom boundary is prescribed to be 0.

To investigate the size effect on the indentation, we set the radius of indenters as R=1 nm, 5 nm and 10 nm, respectively. For comparison, we also model the classical transversely isotropic elasticity model (T.Iso.) and the simple homogenization model (S. Homo). Fig. 9b shows the fringe of the third principal strain field distribution of the CM2D model around the indenters (R=1 nm). It's evident that compression strain will concentrate near the contact surface, and decays quickly away from it.

Fig. 9c exhibits the force-depth curves for various material models with various indenter radii. For the T.Iso. model, the force-depth curve (yellow lines in Fig. 9c) matches well the power function model $P = a h_i^m$ usually used to fit the unloading curves in indentation tests(Oliver and Pharr, 1992). And the inferred reduced modulus of the T.Iso. (yellow lines in Fig. 9d) matches extremely well with the classical prediction given by Eq. (24), regardless of the various indenter radii and indentation depths.

By contrast, the force-depth data of the S.Homo. (red lines in Fig. 9c) and the CM2D (blue lines in Fig. 9c) models deviate from the power function curve and the reduced moduli from the classical prediction, when h_i is relatively small. The forces needed for the same indenter to reach the same depth increase as the monolayer bending effect and surface layer effect are added in turn, because both of them increase the stiffness of materials. This is also reflected in the reduced moduli, as shown in Fig. 9d. As the depth increases sufficiently, both the force and the reduced modulus curves merge with their counterparts of the T.Iso. Hence, there is a size effect with respect to the standard indentation model. Moreover, this size effect becomes even stronger as the radius of the indenter decreases. It should be noted that the process we discussed above is purely elastic. Therefore, the size effect identified here is different from what has been reported before, which is mainly caused by dislocation and plasticity (e.g., (Nix and Gao, 1998; Pharr et al., 2010; Danas et al., 2012)). Furthermore, we also validate the modeling of indentation by MD simulations (detailed in S4 of the Supplementary Information). The obtained indentation force-depth curves (Fig.S4c), as well as the deformation of top surface (Fig.S4d) are comparable to their counterparts predicted by CM2D model.

To understand this size effect, let's first consider simplified cases, i.e., the indentations of suspended membrane and beam (Fig. 10a). When a suspended membrane is indented by an indenter, it will fit the shape of the indenter within the contact surface and departs with the indenter at the contact edge tangential to the indenter, because a membrane cannot resist bending. By contrast, the bending rigidity of a beam won't allow it to fit the indenter as well as a membrane does. The curvature of a beam must be continuous. Compared with a membrane, the contact area shrinks yet the bending rigidity requires the beam to keep a lower profile even outside the contact area, as if it was indented by an even larger indenter, as indicated by the black dot line in Fig. 10a.

In some sense, the T.Iso. model is similar to a membrane, while the CM2D and S.Homo. models to the beam. The profiles of the indenter tip and top boundaries of specimens shown by the inset in Fig. 10b confirm this similarity. Indeed, as shown in Fig. 10b, the contour of displacement field w along the indentation direction of the T.Iso. model is more concentrated, followed by the S.Homo. model, and then the CM2D model. For example, the $w/R = 0.04$ line of the CM2D model can be nearly three times far away from the indenter tip than that of the T.Iso. model. The line of the S.Homo. model sits between the two near the top boundary and is much closer to that of the T.Iso. model. So, the monolayer bending effect does make the CM2D and S.Homo. models appear to be indented by larger indenters, leading to more area near the contact line being compressed. This accounts for the upward-shifted curves of indentation forces and reduced moduli of the CM2D and S.Homo. models. Besides, this also suggests that without monolayer bending effect, the size effect will be lost, and without surface layer effect, the size effect will be suppressed to a large extent.

As the indenter is pressed into the specimen by a sufficiently large depth, the indentation force increases sharply, resulting in a significant response from the specimen. The top boundary is forced by the below material volume of the specimen to contact closely with the indenter or even partly warp it. The monolayer bending effect caused as-if-a-larger-indenter effect dies away. Consequently, the contours of displacement fields approach each other and the corresponding top boundary profiles become hard to distinguish (see Fig. 10c and its inset). Besides, due to the increasing depth, the highly deformed volume expands and more layers become actively involved in the deformation to a large extent, which further dwarfs the effect of monolayer sheet bending rigidity. Therefore, the curves of indentation forces and reduced moduli of the CM2D and S.Homo. models gradually converge with those of the T.Iso. model and the size effect becomes insignificant.

Based on the above analyses, we can conclude that a smaller indenter radius manifests the size effect through at least two aspects. On the one hand, a smaller radius itself renders an even stronger curvature, which magnifies the monolayer bending effect, because the specimen is forced to fit with the shape of the indenter on the contact surface. This will lead to the upward shift of the curves of force and reduced modulus when the depth is relatively small as shown in Fig. 9c and d. On the other hand, the indenter needs to be pressed
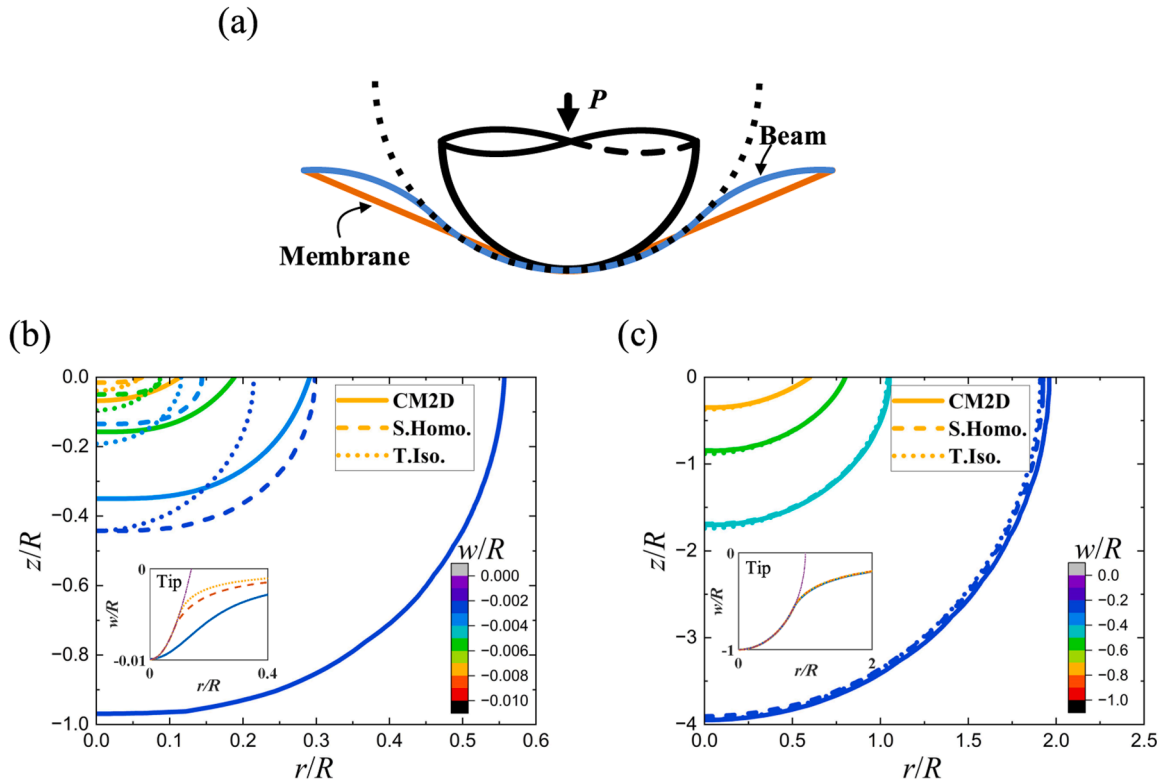
Fig. 10. (a) Schematic illustration of bending deformation modes for suspended membrane and beam under indentation, respectively. Contours of the normalized displacement field along the indentation direction when (b) $h_i/R = 0.01$ and (c) $h_i/R = 1$. The solid line, dash line and dot line represent the CM2D, S.Homo and T.Iso. models, respectively. The insets in (b) and (c) give the corresponding profiles of the indenter tip and the top boundaries of the specimens.

relatively deeper so that sufficient pressure can be accumulated and the top boundary can be forced to embrace the smaller indenter. This delays the merging of the force and reduced modulus curves, and thus, enlarges the range of depth dependence.

4. Discussion on the monolayer bending and surface layer effects

The above analysis indicates that the CM2D framework can be easily transferred to specific mechanical problems, such as beam, plate and indentation. However, we are still limited to specific materials and have not systematically analyzed the monolayer bending and surface layer effects. As the bulging test is ubiquitous in nano-experiments(Wang et al., 2017, 2019; Yue et al., 2012; Cui et al., 2023), in this section, we take the uniformly loaded circular plate as an example to study the two special effects of 2D materials so that we can take the bending rigidity as an indicator for the convenience of discussion.
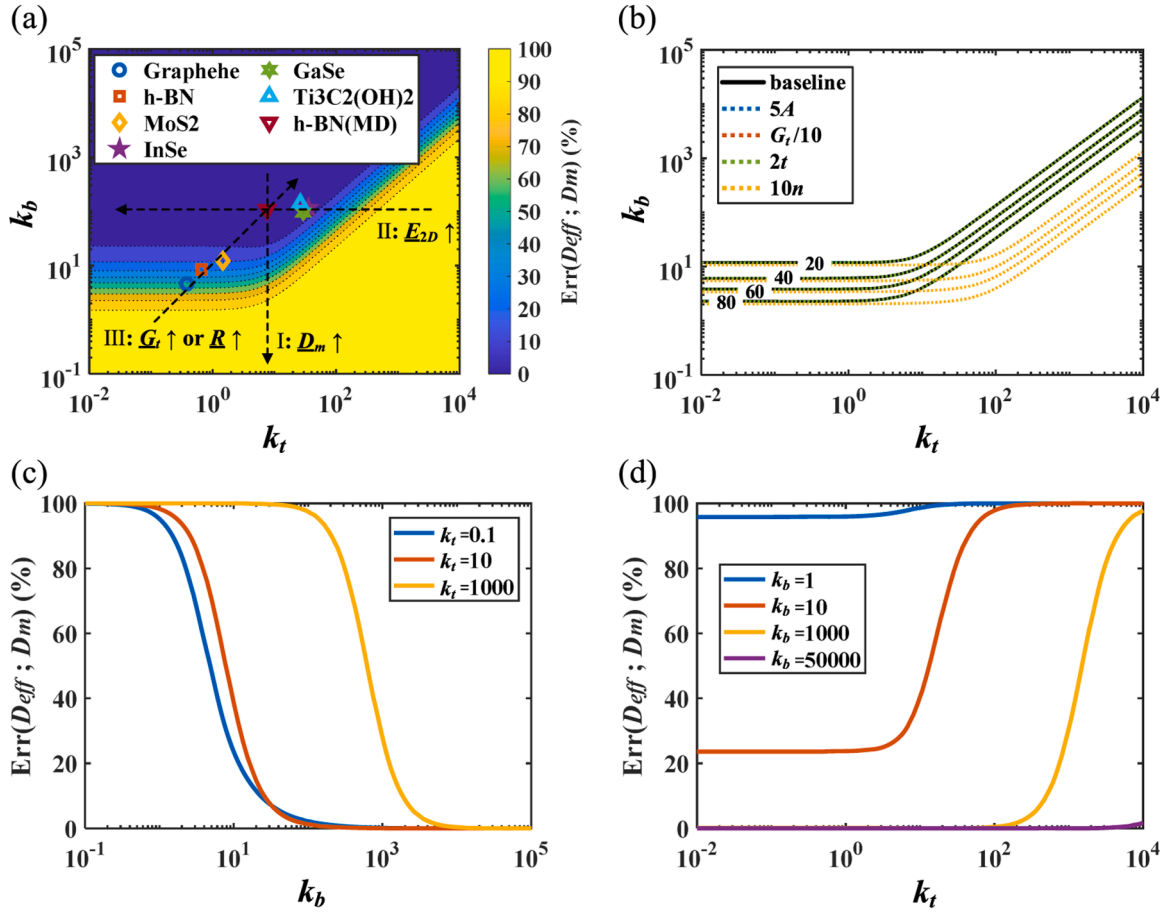
4.1. Monolayer bending effect

To measure the monolayer bending effect, we define

$$Err(D_{eff}; D_m) = \frac{D_{eff} - D_{eff,D_m}}{D_{eff}} \times 100\% \tag{26}$$

as the relative error caused by neglecting this effect, where D_{eff} is the effective bending rigidity of the CM2D plates as defined by Eq. (21) and D_{eff,D_m} can be obtained as the effective bending rigidity of the CM2D plate model with $D_m = 0$.

Fig. 11a illustrates the contour plot of $Err(D_{eff}; D_m)$ given in the k_b, k_t coordinate system, with baseline parameters $n = 5$, A = 20, t=0.3201 nm and G_t=7.655 GPa. It's evident that $Err(D_{eff}; D_m)$ varies rapidly in a ribbon-like zone, where the contour lines are

Fig. 11. (a) The contour over k_b and k_t of relative error $Err(D_{eff}; D_m)$ brought by neglecting the monolayer bending effect with $n = 5$. The positions of several 2D materials are marked, whose parameters can be found on Table.S1. The dashed arrows I~III indicate the evolution paths of contour points as the corresponding normalized parameter increases. (b) The variation of contour lines upon various parameters with baseline $n = 5$, A = 20, $t = 0.3201$ nm, and $G_t = 7.655$ GPa. Variation of $Err(D_{eff}; D_m)$ as a function of (c) k_b with $k_t = 0.1, 10, 1000$ and (d) k_t with $k_b = 1, 10, 1000, 50000$.

crowded together. By varying these baseline parameters, it's found that the contour lines don't move when A, t or G_t varies, but they shift toward the large $Err(D_{eff}; D_m)$ zone as n increases (Fig. 11b), though the extreme values of $Err(D_{eff}; D_m)$ are maintained. In other words, $Err(D_{eff}; D_m)$ remains constant so long as k_b, k_t and n reamin unchanged, and it decreases as n increase.

As shown in Fig. 11c, $Err(D_{eff}; D_m)$ decreases, i.e. the importance of monolayer bending effect is undermined, as k_b increases upon constant k_t and n. On the one hand, the increase in $k_b = R/l_b$ with a constant R means a decreasing bending-shear characteristic length $l_b = \sqrt{D_m/G_t t}$, which can be caused by either a smaller monolayer bending rigidity D_m or a larger interlayer shear stiffness $G_t t$. Obviously, a smaller D_m itself means a weaker monolayer bending effect. And strong interlayer shear stiffness can encourage the intralayer deformation mode by efficiently transferring loads between adjacent layers, as mentioned in Section 3.2.3, which dwarfs the contribution of monolayer bending rigidity to the overall bending resistance and thus weakens the monolayer bending effect. On the other hand, if it is the increase in R that drives k_b to increase while $k_t = R/l_t$ remain unchanged, then $l_t = \sqrt{E_{2D} t/\left(1 - \nu_p^2\right) G_t}$ will have to increase, leading to a relatively strong intralayer stretch resistance. As a result, the contribution of monolayer bending rigidity is also decreased, impairing the monolayer bending effect.

On the contrary, the increase in k_t, upon constant k_b and n, can manifest the monolayer bending effect. As shown in Fig. 11d, $Err(D_{eff}; D_m)$ increases with k_t for a given k_b. When R remains constant, k_t increases upon decreasing l_t, which leads to a relatively weak intralayer stretch resistance and thus makes the monolayer bending rigidity more important. When R drives k_t to increase while k_b remain constant, l_b will increase, which means a relatively strong monolayer bending rigidity and thus manifests the monolayer bending effect.

We have discussed the variation of $Err(D_{eff}; D_m)$ as functions of dimensionless parameters n, k_b and k_t, respectively. To give a more straightforward account, we shall discuss $Err(D_{eff}; D_m)$ upon the modulation of one specific parameter each time, like D_m, E_{2D}, G_t or R.
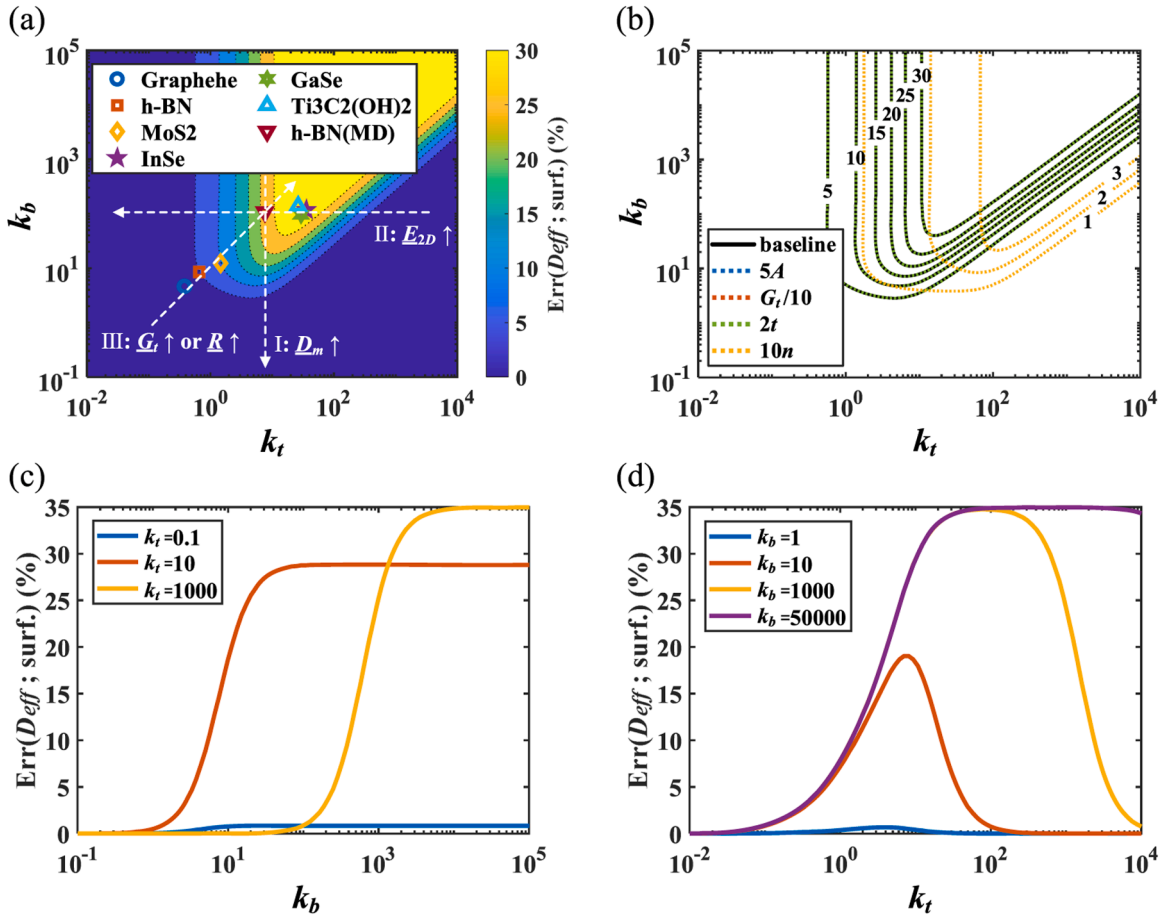
Fig. 12. (a) The contour over k_b and k_t of relative error $Err(D_{eff}; surf.)$ brought by neglecting the monolayer bending effect with $n = 5$. The positions of several 2D materials are marked, whose parameters can be found on Table.S1. The dashed arrows I~III indicate the evolution paths of contour points as the corresponding normalized parameter increases. (b) The variation of contour lines upon various parameters with baseline $n = 5$, $A = 20$, $t = 0.3201$ nm, and $G_t = 7.655$ GPa. Variation of $Err(D_{eff}; surf.)$ as a function of (c) k_b with $k_t = 0.1, 10, 1000$ and (d) k_t with $k_b = 1, 10, 1000, 50000$.

For the convenience of discussion, we normalize all the adjusted parameters by the corresponding baseline parameters of 5 layer h-BN with radius R_0=25.6 nm (i.e., see Table.S1 and Fig. 11a for details). The normalized parameters are distinguished by underlines. For example, when only the radius R is adjusted, we have the normalized parameter $\underline{R} = R/R_0$.

As shown in Fig.S3a, an increase in $\underline{D_m}$ obviously represents more important monolayer bending effect, leading to the increase in $Err(D_{eff}; D_m)$. Besides, considering $k_b \propto 1/\sqrt{D_m}$, an increase in $\underline{D_m}$ will exclusively reduce k_b, which also induces the increase in $Err(D_{eff}; D_m)$, reflected by the dashed arrow I in Fig. 11a . On the contrary, the increase in $\underline{E_{2D}}$, $\underline{G_t}$ or $\underline{R}$ causes the decrease in $Err(D_{eff}; D_m)$, because each of them promotes the contribution of intralayer deformation resistance to overall bending rigidity. This is self-evident for $\underline{E_{2D}}$. And as discussed in Section 3.2.3 and 3.2.4, either an increase in $\underline{G_t}$ or $\underline{R}$ will promote the interlayer load transfer, thus amplifying the significance of the intralyer stiffness, which in turn diminishes the contribution of monolayer bending rigidity. In terms of the dimensionless parameters k_b and k_t, an increase in $\underline{E_{2D}}$ can exclusively decrease k_t ($\propto 1/\sqrt{E_{2D}}$), reflected by the dashed arrow II in Fig. 11a, which leads to an decrease in $Err(D_{eff}; D_m)$. In addition, considering $k_t, k_b \propto R\sqrt{G_t}$, an increase in either $\underline{G_t}$ or $\underline{R}$ will increase k_b and k_t proportionally, represented by the dashed arrow III with a slope of 45° in Fig. 11a, which also indicates an decrease in $Err(D_{eff}; D_m)$.

Furthermore, several typical 2D materials (parameters listed in Table.S1) are marked in Fig. 11a. For a specific material, the characteristic lengths l_t, l_b is fixed. Then, the two dimensionless coefficients $k_t = R/l_t, k_b = R/l_b$ only depend on radius R. Thus, the monolayer bending effect only depends on the deformation length scale R and layer number n. To show this, we plot the contour of $Err(D_{eff}; D_m)$ over n and the monolayer aspect ratio $\alpha = R/t$ for graphene and InSe as two typical examples (Fig.S5a and S5c in the Supplementary Information). The contour lines serve as the critical lines of n and α, beyond which neglecting the monolayer bending effect would cause error no more than the corresponding contour line values.

4.2. Surface layer effect

Similarly, as a measurement of the surface layer effect, we define the relative error caused by neglecting it, i.e.,

$$Err(D_{eff}; surf.) = \frac{D_{eff} - D_{eff,S.Homo.}}{D_{eff}} \times 100\% \tag{27}$$

where $D_{eff,S.Homo.}$ is the effective bending rigidity of the S.Homo. model defined similar to Eq. (21).

Fig. 12a illustrates the contour plot of $Err(D_{eff}; surf.)$ as a function of k_b and k_t, under the same baseline parameters as in Section 4.1. It's evident that $Err(D_{eff}; surf.)$ also varies rapidly within a narrow ribbon-like zone, but with a sharp corner. The contour lines stay still as A, t or G_t changes (Fig. 12b). When n increases, not only the contour lines shift rightward, but also their values decrease. For example, the values of contour lines decrease by an order of magnitude when n increases from 5 to 50. This suggests that the surface layer effect becomes weak quickly as n increases, which is obvious because the specific surface area decreases. When n is sufficiently large, the surface layer effect can be neglected. For example, on the scenario of Fig. 12b, neglecting the surface layer effect only causes an error of less than 4%.

As shown in Fig. 12c, $Err(D_{eff}; surf.)$ increases with k_b. This is because the surface layer effect is directly related to the contribution of the intralayer deformation of the outmost layers to the overall bending deformation. When k_b increases with a fixed R, l_b decreases, suggesting a relatively large interlayer shear resistance for interlayer load transfer during bending. Thus, the outmost layers play a more important role, manifesting the surface layer effect. On the other hand, if R increases, l_t will increase to keep k_t constant, resulting a relatively large intralayer stiffness. Then, the surface layer effect is also magnified.

When k_t increases, $Err(D_{eff}; surf.)$ increases at first, and then decreases finally, between which there will be a plateau if k_b is large enough (Fig. 12d). The increase in k_t originates from the relative decrease in l_t. When l_t is relatively large, the intralayer stiffness is relatively large. It is hard for Interlayer shear force to stretch or compress individual layers. Deformation mainly happens through monolayer bending and interlayer shearing. Thus, the outmost layer intralayer stiffness becomes insignificant. As the intralayer stiffness relatively reduces, the intralayer deformation becomes important, and so is the stiffness of the outmost layer. But if the intralayer stiffness keeps diminishing compared to interlayer shear stiffness, it will enter a zone where intralayer deformation mode is so flexible that the corresponding stiffness becomes unimportant. Hence, the surface layer effect has a non-monotonic trend upon the increase in k_t.

Similarly, we also discuss $Err(D_{eff}; surf.)$ upon the modulation of one specific parameter each time. The same set of baseline parameters are employed, as well as the same definition of normalized parameters. As shown in Fig.S3b, an increase in $\underline{D_m}$ will promote the contribution of monolayer bending rigidity to the overall bending rigidity and in turn dwarf that of the outmost layers, which can also be reflected by a decreasing trend of $Err(D_{eff}; surf.)$ following the dashed arrow I in Fig. 12a. Besides, an increase in $\underline{E_{2D}}$ leads to the increase and then decrease in $Err(D_{eff}; surf.)$. That is because, the influence of intralayer stiffness gradually increases as $\underline{E_{2D}}$ increases from small values. However, when $\underline{E_{2D}}$ is big enough, the intralayer stiffness becomes so strong that the interlayer load transfer becomes the bottleneck. In other words, the stronger the intralayer stiffness is, the harder for interlayer to transfer load. As a result, the influence of surface layer effect decreases as $\underline{E_{2D}}$ further increases, which can also be reflected by the dashed arrow II in Fig. 12a. In addition, an increase in either $\underline{G_t}$ or $\underline{R}$ will promote the interlayer load transfer, and thus amplify the significance of the intralayer stiffness. Therefore, the surface layer effect becomes more pronounced. The dashed arrow III with a slope of 45° in Fig. 12a also shows an increase trend of $Err(D_{eff}; surf.)$ with an increase in either $\underline{G_t}$ or $\underline{R}$.

Moreover, several typical 2D materials (parameters listed in Table.S1) are also marked in Fig. 12a. Obviously, for a specific material, the surface layer effect also only depends on the deformation length scale R and layer number n. To show this, we plot the contour of $Err\left(D_{eff}; surf.\right)$ over n and the monolayer aspect ratio $\alpha = R/t$ for graphene and InSe as two typical examples (Fig.S5b and S5d in the Supplementary Information). The contour lines serve as the critical lines of n and α, beyond which neglecting the surface layer effect would cause error no more than the corresponding contour line values.

5. Conclusion remarks

In this work, we present a general 3D continuum mechanics framework for 2D Materials (CM2D), which is transversely isotropic, integrating monolayer bending and surface layer effects. All the constitutive parameters of the CM2D model have well-defined physical meanings and can be directly measured in experiments or atomic simulations. Under the framework of CM2D, the mechanical behaviors of beam-like, plate-like deformation and indention of 2D materials are studied. The main findings are as follows:

(1) The overall bending deformation modes of both 2D material beams and plates are controlled by the competition between the intralayer deformation mode and interlayer shear deformation mode.
(2) For beams and circular plates, the bending rigidity can be fully characterized by four dimensionless parameters, i.e., tension-shear coefficient k_t, bend-shear coefficient k_b, geometrical aspect ratio α and number of layers n.
(3) The size effect on the indentation of 2D materials emerging at the pure elastic deformation regime is identified, distinct from the size effect caused by plasticity.
(4) The monolayer bending and surface layer effects play an important role in the mechanical behaviors of 2D materials, which only depends on the three dimensionless parameters, i.e., k_t, k_b and n.

Note that we intend to present a framework to formulate a more general 3D continuum mechanics model for 2D materials, so the focus is limited to small deformation scale to keep the model straightforward. The main challenge of extending the present model to account for finite deformation is to develop a proper interlayer constitutive relationship by taking the interlayer sliding into consideration, which will be addressed in our future work. Hopefully, such extended model can quantitatively account for the relationship between sliding and bending, and thus the bending induced softening observed in experiments(Han et al., 2019). Additionally, for general vdW heterostructures stacked in arbitrary order, the continualization from multilayer 2D materials to its multilayer continuum model still hold, where each layer represents an individual sheet of 2D material and each interlayer medium represents different interlayer interactions between various 2D materials. However, internal homogenization of the multilayer continuum model may encounter difficulty due to the arbitrary distribution of various 2D material sheets. Besides, for moiré heterostructures, the moiré in-plane lattice reconstruction regulates out-of-plane moiré morphology, thereby modifying the local registry of stacking status of heterostructures(Huang and Liu, 2024). This could possibly enlarge the period of spatial distribution of local interlayer shear modulus and distance, potentially impairing the accuracy of the current model. Despite this, our 3D continuum mechanics model can not only provide guidance for the mechanics and applications of 2D materials, but also shed light on the physical origin of the strain gradient, high-order moduli, and couple stress in the high-order continuum mechanics theories.

CRediT authorship contribution statement

Huichao Liu: Writing – review & editing, Writing – original draft, Visualization, Validation, Methodology, Investigation, Data curation, Conceptualization. **Yan Chen:** Writing – review & editing, Writing – original draft, Validation, Supervision, Methodology, Funding acquisition, Conceptualization. **Wen Wang:** Writing – review & editing, Visualization, Validation, Methodology. **Luqi Liu:** Writing – review & editing, Visualization, Validation, Investigation. **Yilun Liu:** Writing – review & editing, Visualization, Validation, Project administration, Investigation, Funding acquisition, Conceptualization. **Quanshui Zheng:** Writing – review & editing, Validation, Supervision, Investigation.

Declaration of competing interest

The authors declare that they have no known competing financial interests or personal relationships that could have appeared to influence the work reported in this paper.

Acknowledgments

Supplementary materials

Supplementary material associated with this article can be found, in the online version, at doi:10.1016/j.jmps.2024.105911.

Data availability

Data will be made available on request.

References

Akinwande, D., Brennan, C.J., Bunch, J.S., Egberts, P., Felts, J.R., Gao, H., Huang, R., Kim, J.-S., Li, T., Li, Y., Liechti, K.M., Lu, N., Park, H.S., Reed, E.J., Wang, P., Yakobson, B.I., Zhang, T., Zhang, Y.-W., Zhou, Y., Zhu, Y., 2017. A review on mechanics and mechanical properties of 2D materials—Graphene and beyond. Extreme Mech. Lett. 13, 42–77. https://doi.org/10.1016/j.eml.2017.01.008.

Ares, P., Cea, T., Holwill, M., Wang, Y.B., Roldán, R., Guinea, F., Andreeva, D.V., Fumagalli, L., Novoselov, K.S., Woods, C.R., 2020. Piezoelectricity in Monolayer Hexagonal Boron Nitride. Adv. Mater. 32, 1905504. https://doi.org/10.1002/adma.201905504.

Arroyo, M., Belytschko, T., 2004a. Finite crystal elasticity of carbon nanotubes based on the exponential Cauchy-Born rule. Phys. Rev. B 69, 115415. https://doi.org/10.1103/PhysRevB.69.115415.

Arroyo, M., Belytschko, T., 2004b. Finite element methods for the non-linear mechanics of crystalline sheets and nanotubes. Int. J. Numer. Methods Eng. 59, 419–456. https://doi.org/10.1002/nme.944.

Arroyo, M., Belytschko, T., 2002. An atomistic-based finite deformation membrane for single layer crystalline films. J. Mech. Phys. Solids 50, 1941–1977. https://doi.org/10.1016/S0022-5096(02)00002-9.

Autere, A., Jussila, H., Dai, Y., Wang, Y., Lipsanen, H., Sun, Z., 2018. Nonlinear Optics with 2D Layered Materials. Adv. Mater. 30, 1705963. https://doi.org/10.1002/adma.201705963.

Cao, Y., Fatemi, V., Fang, S., Watanabe, K., Taniguchi, T., Kaxiras, E., Jarillo-Herrero, P., 2018. Unconventional superconductivity in magic-angle graphene superlattices. Nature 556, 43–50. https://doi.org/10.1038/nature26160.

Chen, X., Yi, C., Ke, C., 2015. Bending stiffness and interlayer shear modulus of few-layer graphene. Appl. Phys. Lett. 106, 101907. https://doi.org/10.1063/1.4915075.

Chen, Y., Liu, H., Pang, K., Zhang, C., Qin, H., Xu, Z., Liu, Y., 2023. Bending deformable tension-shear model for nacre-like composites. J. Mech. Phys. Solids 171, 105132. https://doi.org/10.1016/j.jmps.2022.105132.

Chen, Y., Ouyang, W., Zhou, K., Qin, H., Liu, Y., 2022. Finite temperature mechanics of multilayer 2D materials. Extreme Mech. Lett. 52, 101612. https://doi.org/10.1016/j.eml.2022.101612.

Cui, X., Dong, W., Feng, S., Wang, G., Wang, C., Wang, S., Zhou, Y., Qiu, X., Liu, L., Xu, Z., Zhang, Z., 2023. Extra-High Mechanical and Phononic Anisotropy in Black Phosphorus Blisters. Small., e2301959 https://doi.org/10.1002/smll.202301959.

Dai, Z., Liu, L., Zhang, Z., 2019. Strain Engineering of 2D Materials: issues and Opportunities at the Interface. Adv. Mater. 31, 1805417. https://doi.org/10.1002/adma.201805417.

Danas, K., Deshpande, V.S., Fleck, N.A., 2012. Size effects in the conical indentation of an elasto-plastic solid. J. Mech. Phys. Solids 60, 1605–1625. https://doi.org/10.1016/j.jmps.2012.05.002.

Davini, C., Favata, A., Paroni, R., 2017. The Gaussian stiffness of graphene deduced from a continuum model based on Molecular Dynamics potentials. J. Mech. Phys. Solids 104, 96–114. https://doi.org/10.1016/j.jmps.2017.04.003.

Delafargue, A., Ulm, F.-J., 2004. Explicit approximations of the indentation modulus of elastically orthotropic solids for conical indenters. Int. J. Solids Struct. 41, 7351–7360. https://doi.org/10.1016/j.ijsolstr.2004.06.019.

Deng, Y., Yu, Y., Shi, M.Z., Guo, Z., Xu, Z., Wang, J., Chen, X.H., Zhang, Y., 2020. Quantum anomalous Hall effect in intrinsic magnetic topological insulator MnBi2Te4. Science (1979) 367, 895–900. https://doi.org/10.1126/science.aax8156.

DiBiasio, C.M., Cullinan, M.A., Culpepper, M.L., 2007. Difference between bending and stretching moduli of single-walled carbon nanotubes that are modeled as an elastic tube. Appl. Phys. Lett. 90, 203116. https://doi.org/10.1063/1.2741144.

Du, L., Hasan, T., Castellanos-Gomez, A., Liu, G.-B., Yao, Y., Lau, C.N., Sun, Z., 2021. Engineering symmetry breaking in 2D layered materials. Nat. Rev. Phys. 3, 193–206. https://doi.org/10.1038/s42254-020-00276-0.

Fleck, N.A., Hutchinson, J.W., 1997. Strain Gradient Plasticity. In: Hutchinson, John W., Wu, T.Y. (Eds.), Advances in Applied Mechanics. Elsevier, pp. 295–361. https://doi.org/10.1016/S0065-2156(08)70388-0.

Geim, A.K., Grigorieva, I.V., 2013. Van der Waals heterostructures. Nature 499, 419–425. https://doi.org/10.1038/nature12385.

Gere, J.M., Timoshenko, S.P., 1995. Mechanics of materials, 3. SI ed., reprinted. ed. Chapman & Hall, London.

Ghosh, S., Arroyo, M., 2013. An atomistic-based foliation model for multilayer graphene materials and nanotubes. J. Mech. Phys. Solids 61, 235–253. https://doi.org/10.1016/j.jmps.2012.07.002.

Guo, X., Wang, J.B., Zhang, H.W., 2006. Mechanical properties of single-walled carbon nanotubes based on higher order Cauchy–Born rule. Int. J. Solids Struct. 43, 1276–1290. https://doi.org/10.1016/j.ijsolstr.2005.05.049.

Gurtin, M.E., Ian Murdoch, A., 1975. A continuum theory of elastic material surfaces. Arch. Ration. Mech. Anal. 57, 291–323. https://doi.org/10.1007/BF00261375.

Hadjesfandiari, A.R., Dargush, G.F., 2011. Couple stress theory for solids. Int. J. Solids Struct. 48, 2496–2510. https://doi.org/10.1016/j.ijsolstr.2011.05.002.

Han, E., Yu, J., Annevelink, E., Son, J., Kang, D.A., Watanabe, K., Taniguchi, T., Ertekin, E., Huang, P.Y., van der Zande, A.M., 2019. Ultrasoft slip-mediated bending in few-layer graphene. Nat. Mater. https://doi.org/10.1038/s41563-019-0529-7.

He, Z., Zhu, Y., Xia, J., Wu, H., 2019. Optimization design on simultaneously strengthening and toughening graphene-based nacre-like materials through noncovalent interaction. J. Mech. Phys. Solids 133, 103706. https://doi.org/10.1016/j.jmps.2019.103706.

Hou, Y., Zhou, J., He, Z., Chen, J., Zhu, M., Wu, H., Lu, Y., 2024. Tuning instability in suspended monolayer 2D materials. Nat. Commun. 15, 4033. https://doi.org/10.1038/s41467-024-48345-7.

Huang, K., Liu, Y., 2024. A general mechanism for long-range friction modulation in graphene-based moiré heterostructures. J. Mech. Phys. Solids 185, 105560. https://doi.org/10.1016/j.jmps.2024.105560.

Huang, Y., Wu, J., Hwang, K.C., 2006. Thickness of graphene and single-wall carbon nanotubes. Phys. Rev. B 74, 245413. https://doi.org/10.1103/PhysRevB.74.245413.

Huang, Z., He, Z., Zhu, Y., Wu, H., 2023. A general theory for the bending of multilayer van der Waals materials. J. Mech. Phys. Solids 171, 105144. https://doi.org/10.1016/j.jmps.2022.105144.

Huang, Z.P., Wang, J., 2006. A theory of hyperelasticity of multi-phase media with surface/interface energy effect. Acta Mech. 182, 195–210. https://doi.org/10.1007/s00707-005-0286-3.

Javili, A., McBride, A., Steinmann, P., 2013. Thermomechanics of Solids With Lower-Dimensional Energetics: on the Importance of Surface, Interface, and Curve Structures at the Nanoscale. A Unifying Review. Appl. Mech. Rev. 65. https://doi.org/10.1115/1.4023012.

Kim, S.E., Mujid, F., Rai, A., Eriksson, F., Suh, J., Poddar, P., Ray, A., Park, C., Fransson, E., Zhong, Y., Muller, D.A., Erhart, P., Cahill, D.G., Park, J., 2021. Extremely anisotropic van der Waals thermal conductors. Nature 597, 660–665. https://doi.org/10.1038/s41586-021-03867-8.

Kınacı, A., Haskins, J.B., Sevik, C., Çağın, T., 2012. Thermal conductivity of BN-C nanostructures. Phys. Rev. B 86, 115410. https://doi.org/10.1103/PhysRevB.86.115410.

Koskinen, P., Kit, O.O., 2010. Approximate modeling of spherical membranes. Phys. Rev. B 82, 235420. https://doi.org/10.1103/PhysRevB.82.235420.

Lamuta, C., 2019. Elastic constants determination of anisotropic materials by depth-sensing indentation. SN Appl. Sci. 1, 1263. https://doi.org/10.1007/s42452-019-1301-y.

Lee, C., Wei, X., Kysar, J.W., Hone, J., 2008. Measurement of the Elastic Properties and Intrinsic Strength of Monolayer Graphene. Science (1979) 321, 385–388. https://doi.org/10.1126/science.1157996.

Li, B., Tan, M., Shen, C., Long, Y., Gao, Z., Wang, J., Guo, W., Yin, J., 2024. Bending stiffness of ionically bonded mica multilayers told by its bubbles. J. Mech. Phys. Solids 190, 105723. https://doi.org/10.1016/j.jmps.2024.105723.

Li, S., Li, Q., Carpick, R.W., Gumbsch, P., Liu, X.Z., Ding, X., Sun, J., Li, J., 2016. The evolving quality of frictional contact with graphene. Nature 539, 541–545. https://doi.org/10.1038/nature20135.

Liu, Y., Weiss, N.O., Duan, Xidong, Cheng, H.-C., Huang, Y., Duan, Xiangfeng, 2016. Van der Waals heterostructures and devices. Nat. Rev. Mater. 1, 1–17. https://doi.org/10.1038/natrevmats.2016.42.

Liu, Y., Xie, B., Zhang, Z., Zheng, Q., Xu, Z., 2012. Mechanical properties of graphene papers. J. Mech. Phys. Solids 60, 591–605. https://doi.org/10.1016/j.jmps.2012.01.002.

Liu, Y., Xu, Z., 2014. Multimodal and self-healable interfaces enable strong and tough graphene-derived materials. J. Mech. Phys. Solids 70, 30–41. https://doi.org/10.1016/j.jmps.2014.05.006.

Liu, Y., Xu, Z., Zheng, Q., 2011. The interlayer shear effect on graphene multilayer resonators. J. Mech. Phys. Solids 59, 1613–1622. https://doi.org/10.1016/j.jmps.2011.04.014.

Liu, Z., Yang, J., Grey, F., Liu, J.Z., Liu, Y., Wang, Y., Yang, Y., Cheng, Y., Zheng, Q., 2012. Observation of Microscale Superlubricity in Graphite. Phys. Rev. Lett. 108, 205503. https://doi.org/10.1103/PhysRevLett.108.205503.

Lu, Q., Arroyo, M., Huang, R., 2009. Elastic bending modulus of monolayer graphene. J. Phys. Appl. Phys. 42, 102002. https://doi.org/10.1088/0022-3727/42/10/102002.

Lu, W.B., Wu, J., Jiang, L.Y., Huang, Y., Hwang, K.C., Liu, B., 2007. A cohesive law for multi-wall carbon nanotubes. Philos. Mag. 87, 2221–2232. https://doi.org/10.1080/14786430701344558.

Ma, X., Liu, L., Zhang, Z., Wei, Y., 2022. Bending Stiffness of Circular Multilayer van der Waals Material Sheets. J. Appl. Mech. 89. https://doi.org/10.1115/1.4053494.

Ma, X., Liu, L., Zhang, Z., Wei, Y., 2020. A Method to Determine the Geometry-Dependent Bending Stiffness of Multilayer Graphene Sheets. J. Appl. Mech. 88. https://doi.org/10.1115/1.4048571.

Mindlin, R.D., Eshel, N.N., 1968. On first strain-gradient theories in linear elasticity. Int. J. Solids Struct. 4, 109–124. https://doi.org/10.1016/0020-7683(68)90036-X.

Mozaffari, K., Yang, S., Sharma, P., 2020. Surface Energy and Nanoscale Mechanics. In: Andreoni, W., Yip, S. (Eds.), Handbook of Materials Modeling: Applications: Current and Emerging Materials. Springer International Publishing, Cham, pp. 1949–1974. https://doi.org/10.1007/978-3-319-44680-6_48.

Neff, P., Münch, I., Ghiba, I.-D., Madeo, A., 2016. On some fundamental misunderstandings in the indeterminate couple stress model. A comment on recent papers of A.R. Hadjesfandiari and G.F. Dargush. Int. J. Solids Struct. 81, 233–243. https://doi.org/10.1016/j.ijsolstr.2015.11.028.

Nix, W.D., Gao, H., 1998. Indentation size effects in crystalline materials: a law for strain gradient plasticity. J. Mech. Phys. Solids 46, 411–425. https://doi.org/10.1016/S0022-5096(97)00086-0.

Novoselov, K.S., Mishchenko, A., Carvalho, A., Neto, A.H.C., 2016. 2D materials and van der Waals heterostructures. Science (1979) 353. https://doi.org/10.1126/science.aac9439.

Oliver, W.C., Pharr, G.M., 2010. Nanoindentation in materials research: past, present, and future. MRS Bull 35, 897–907. https://doi.org/10.1557/mrs2010.717.

Oliver, W.C., Pharr, G.M., 1992. An improved technique for determining hardness and elastic modulus using load and displacement sensing indentation experiments. J. Mater. Res. 7, 1564–1583. https://doi.org/10.1557/JMR.1992.1564.

Ouyang, W., Mandelli, D., Urbakh, M., Hod, O., 2018. Nanoserpents: graphene Nanoribbon Motion on Two-Dimensional Hexagonal Materials. Nano Lett. 18, 6009–6016. https://doi.org/10.1021/acs.nanolett.8b02848.

Pharr, G.M., Herbert, E.G., Gao, Y., 2010. The Indentation Size Effect: a Critical Examination of Experimental Observations and Mechanistic Interpretations. Annu. Rev. Mater. Res. 40, 271–292. https://doi.org/10.1146/annurev-matsci-070909-104456.

Pharr, G.M., Oliver, W.C., Brotzen, F.R., 1992. On the generality of the relationship among contact stiffness, contact area, and elastic modulus during indentation. J. Mater. Res. 7, 613–617. https://doi.org/10.1557/JMR.1992.0613.

Qin, H., Yan, Y., Liu, H., Liu, J., Zhang, Y.-W., Liu, Y., 2020. Modified Timoshenko beam model for bending behaviors of layered materials and structures. Extreme Mech. Lett. 39, 100799. https://doi.org/10.1016/j.eml.2020.100799.

Rafii-Tabar, H., Ghavanloo, E., Fazelzadeh, S.A., 2016. Nonlocal continuum-based modeling of mechanical characteristics of nanoscopic structures. Phys. Rep. 638, 1–97. https://doi.org/10.1016/j.physrep.2016.05.003.

Ru, C.Q., 2000. Effective bending stiffness of carbon nanotubes. Phys. Rev. B 62, 9973–9976. https://doi.org/10.1103/PhysRevB.62.9973.

Shaat, M., Ghavanloo, E., Fazelzadeh, S.A., 2020. Review on nonlocal continuum mechanics: physics, material applicability, and mathematics. Mech. Mater. 150, 103587. https://doi.org/10.1016/j.mechmat.2020.103587.

Shen, Y., Wu, H., 2012. Interlayer shear effect on multilayer graphene subjected to bending. Appl. Phys. Lett. 100, 101909. https://doi.org/10.1063/1.3693390.

Shenderova, O.A., Zhirnov, V.V., Brenner, D.W., 2002. Carbon Nanostructures. Crit. Rev. Solid State Mater. Sci. 27, 227–356. https://doi.org/10.1080/10408430208500497.

Sneddon, I.N., 1965. The relation between load and penetration in the axisymmetric boussinesq problem for a punch of arbitrary profile. Int. J. Eng. Sci. 3, 47–57. https://doi.org/10.1016/0020-7225(65)90019-4.

Srinivasa, A.R., Reddy, J.N., 2017. An Overview of Theories of Continuum Mechanics With Nonlocal Elastic Response and a General Framework for Conservative and Dissipative Systems. Appl. Mech. Rev. 69. https://doi.org/10.1115/1.4036723.

Timoshenko, S.P., Woinowsky-Krieger, S., 1976. Theory of plates and shells, 2. ed. ed, Engineering societies monographs. McGraw-Hill, Auckland.

Toupin, R.A., 1962. Elastic materials with couple-stresses. Arch. Ration. Mech. Anal. 11, 385–414.

Wang, C.Y., Zhang, L.C., 2008. A critical assessment of the elastic properties and effective wall thickness of single-walled carbon nanotubes. Nanotechnology. 19, 075705. https://doi.org/10.1088/0957-4484/19/7/075705.

Wang, G., Dai, Z., Wang, Y., Tan, P., Liu, L., Xu, Z., Wei, Y., Huang, R., Zhang, Z., 2017. Measuring Interlayer Shear Stress in Bilayer Graphene. Phys. Rev. Lett. 119, 036101. https://doi.org/10.1103/PhysRevLett.119.036101.

Wang, G., Dai, Z., Xiao, J., Feng, S., Weng, C., Liu, L., Xu, Z., Huang, R., Zhang, Z., 2019. Bending of Multilayer van der Waals Materials. Phys. Rev. Lett. 123, 116101. https://doi.org/10.1103/PhysRevLett.123.116101.

Wang, G.-F., Feng, X.-Q., 2007. Effects of surface elasticity and residual surface tension on the natural frequency of microbeams. Appl. Phys. Lett. 90, 231904. https://doi.org/10.1063/1.2746950.

Wang, L.-F., Zheng, Q.-S., 2007. Extreme anisotropy of graphite and single-walled carbon nanotube bundles. Appl. Phys. Lett. 90, 153113. https://doi.org/10.1063/1.2722057.

Wei, Y., 2001. Particulate size effects in the particle-reinforced metal-matrix composites. Acta Mech. Sin. 17, 45–58. https://doi.org/10.1007/BF02487769.

Wei, Y., Wang, B., Wu, J., Yang, R., Dunn, M.L., 2013. Bending Rigidity and Gaussian Bending Stiffness of Single-Layered Graphene. Nano Lett. 13, 26–30. https://doi.org/10.1021/nl303168w.

Yadav, U., Ghosh, S., 2022. An atomistic-based finite deformation continuum membrane model for monolayer Transition Metal Dichalcogenides. J. Mech. Phys. Solids 105033. https://doi.org/10.1016/j.jmps.2022.105033.

Yang, F., Chong, A.C.M., Lam, D.C.C., Tong, P., 2002. Couple stress based strain gradient theory for elasticity. Int. J. Solids Struct. 39, 2731–2743. https://doi.org/10.1016/S0020-7683(02)00152-X.

Yu, J., Han, E., Hossain, M.A., Watanabe, K., Taniguchi, T., Ertekin, E., van der Zande, A.M., Huang, P.Y., 2021. Designing the Bending Stiffness of 2D Material Heterostructures. Adv. Mater. 33, 2007269. https://doi.org/10.1002/adma.202007269.

Yuan, W., Ding, Y., Wang, G., 2023. Universal contact stiffness of elastic solids covered with tensed membranes and its application in indentation tests of biological materials. Acta Biomater. 171, 202–208. https://doi.org/10.1016/j.actbio.2023.09.006.

Yue, K., Gao, W., Huang, R., Liechti, K.M., 2012. Analytical methods for the mechanics of graphene bubbles. J. Appl. Phys. 112, 083512. https://doi.org/10.1063/1.4759146.

Zhang, D.-B., Akatyeva, E., Dumitrică, T., 2011. Bending Ultrathin Graphene at the Margins of Continuum Mechanics. Phys. Rev. Lett. 106, 255503. https://doi.org/10.1103/PhysRevLett.106.255503.

Zhang, P., Huang, Y., Gao, H., Hwang, K.C., 2002. Fracture Nucleation in Single-Wall Carbon Nanotubes Under Tension: a Continuum Analysis Incorporating Interatomic Potentials. J. Appl. Mech. 69, 454–458. https://doi.org/10.1115/1.1469002.

Zhang, P., Jiang, H., Huang, Y., Geubelle, P.H., Hwang, K.C., 2004. An atomistic-based continuum theory for carbon nanotubes: analysis of fracture nucleation. J. Mech. Phys. Solids 52, 977–998. https://doi.org/10.1016/j.jmps.2003.09.032.

Zhang, Y., Needleman, A., 2021. Characterization of plastically compressible solids via spherical indentation. J. Mech. Phys. Solids 148, 104283. https://doi.org/10.1016/j.jmps.2020.104283.